Structural insights into F-actin regulation and sarcomere assembly *via* myotilin

Short title: Myotilin-actin complex regulates muscle assembly

Julius Kostan[1,†], Miha Pavšič[2,†], Vid Puž[2], Thomas C. Schwarz[1], Friedel Drepper[3,4], Sibylle Molt[5], Melissa Ann Graewert[6], Claudia Schreiner[1], Sara Sajko[1], Peter F.M. van der Ven[5], Dmitri Svergun[6], Bettina Warscheid[3,4], Robert Konrat[1], Dieter O. Fürst[5], Brigita Lenarčič[2,7,*] and Kristina Djinović-Carugo[1,2,*]

[1] Department of Structural and Computational Biology, Max Perutz Labs, University of Vienna, Campus Vienna Biocenter 5, A-1030 Vienna, Austria

[2] Department of Biochemistry, Faculty of Chemistry and Chemical Technology, University of Ljubljana, Večna pot 5, SI-1000 Ljubljana, Slovenia

[3] Biochemistry and Functional Proteomics, Institute of Biology II, Faculty of Biology, University of Freiburg, 79104, Freiburg, Germany

[4] Signalling Research Centres BIOSS and CIBSS, University of Freiburg, 79104, Freiburg, Germany

[5] Institute for Cell Biology, Department of Molecular Cell Biology, University of Bonn, Ulrich-Haberland-Str. 61a, 53121 Bonn, Germany

[6] European Molecular Biology Laboratory, Hamburg Unit, c/o DESY, Notkestrasse 85, 22607 Hamburg, Germany

[7] Department of Biochemistry, Molecular Biology and Structural Biology, Jozef Stefan Institute, Jamova 39, *SI*-1000 Ljubljana, Slovenia

*Correspondence and requests for materials should be addressed to KDC (kristina.djinovic@univie.ac.at) and/or BL (Brigita.Lenarcic@fkkt.uni-lj.si).

[†]These authors contributed equally to this work

Abstract

Sarcomeres, the basic contractile units of striated muscle cells, contain arrays of thin (actin) and thick (myosin) filaments that slide past each other during contraction. The Ig-like domain containing protein myotilin provides structural integrity to Z-discs - the boundaries between adjacent sarcomeres. Myotilin binds to Z-disc components, including F-actin and α-actinin-2, but the molecular mechanism of binding and implications of these interactions on Z-disc integrity are still elusive. We used a combination of small angle X-ray scattering, cross-linking mass spectrometry, biochemical and molecular biophysics approaches. We discovered that myotilin displays conformational ensembles in solution. We generated a structural model of the F-actin:myotilin complex that revealed how myotilin interacts with and stabilizes F-actin *via* its Ig-like domains and flanking regions. Mutant myotilin designed with impaired F-actin binding showed increased dynamics in cells. Structural analyses and competition assays uncovered that myotilin displaces tropomyosin from F-actin. Our findings suggest a novel role of myotilin as a co-organizer of Z-disc assembly and advance our mechanistic understanding of myotilin's structural role in Z-discs.

Significance Statement

Sarcomeres are the primary structural and functional unit of striated muscles, conferring movement in all animals. The Z-disk is the boundary between adjacent sarcomeres, where actin filaments (F-actin) are anchored. Z-disc protein myotilin, is a scaffold protein, which provides structural integrity to the Z-disc by multiple interactions to its central components, including F-actin and α-actinin-2. Here we provide the structure of myotilin, revealing its structural plasticity in solution and the first integrative structural model of its complex with F-actin. We further show that myotilin displaces tropomyosin from F-actin, implying a novel role of myotilin in sarcomere biogenesis beyond being an interaction hub for Z-disk partners.

KEYWORDS

Sarcomeric Z-disc; F-actin binding; myotilin; α-Actinin; integrative structural model of F-actin/myotilin; competitive tropomyosin binding; Z-disc-assembly regulation;

Highlights

- Myotilin is structurally described as a dynamic ensemble
- Flanking regions enhance F-acting binding to tandem Ig domains
- Integrative structural model of myotilin bound to F-actin
- Myotilin displaces tropomyosin from F-actin, suggesting an organisational role in Z-disc

Introduction

About 40% of the human body is comprised of skeletal muscle, whose contraction leads to locomotion (1). The contractile machinery of cross-striated muscle cells is based on an impressive, almost crystalline array of thin (actin-based) and thick (myosin-based) filaments, arranged in repeating units, the sarcomeres. Stringent control of the precise layout of these filament systems is of utmost importance for efficient conversion of the force produced by the myosin-actin-interaction into contraction at the macroscopic level. Thin filaments are cross-linked in an antiparallel fashion at the Z-discs, the boundaries of adjacent sarcomeres, by multiple molecular interactions (**Figure 1A**). In fact, more than 50 proteins may be associated with mature Z-discs and they are regarded as one of the most complex macromolecular structures in biology. For decades the Z-disc was believed to play a specific role only in sustaining myofibril architecture. This view has changed dramatically within the last decade, with the Z-disc now also being recognized as a prominent hub for signalling, mechanosensing and mechanotransduction, with emerging roles in protein turnover and autophagy (2,3). In line with this, Z-disc proteins have recently been identified as a major phosphorylation hotspot, thereby directly modulating protein interactions and dynamics (4,5).

A striking ultrastructural feature of the Z-disc is its highly ordered, paracrystalline tetragonal arrangement (6). This arrangement is governed by α-actinin-2, which cross-links the overlapping ends of thin filaments of neighbouring sarcomeres and provides structural integrity. α-Actinin-2 also binds to titin, which is connected to thick filaments. This interaction is regulated by a phosphoinositide-based mechanism (7,8). However, many other details of the molecular architecture of the Z-disc remain elusive, and many questions still need to be addressed. For example, why is tropomyosin distributed all along thin filaments of the sarcomere with exception of the Z-disc (6)? How are interactions of α-actinin with numerous binding partners translated into Z-disc assembly?

The Z-disc component myotilin is involved in multiple interactions by directly binding to α-actinin-2, filamin C, FATZ/myozenin/calsarcin, ZASP/cypher and F-actin (9-13). It was therefore identified as a key structural component of Z-discs and proposed to control sarcomere assembly (9-11). Mutations in the human myotilin gene are associated with myofibrillar myopathy (MFM) (14,15), supporting the notion that myotilin is important for proper maintenance, organization and/or function of the Z-disc.

Myotilin is a member of the palladin/myopalladin/myotilin family and contains two Ig domains that are involved in myotilin dimerization, and interact with F-actin and filamin C (**Figure 1B**) (9,10,16,17). The shortest fragment of myotilin that can bind F-actin includes the two Ig domains preceded by a stretch of intrinsically disordered residues (17). A longer myotilin fragment can cross-link actin filaments *in vitro* and *in vivo* (17), and prevents F-actin disassembly induced by latrunculin A (10), revealing its role in stabilization and anchoring of thin filaments in the Z-discs (10). Myotilin dimerization was proposed to form antiparallel dimers with implications for F-actin cross-linking (10), but insight into molecular determinants of myotilin dimerization limited.

To elucidate the molecular mechanism of myotilin interaction with F-actin and the role of this interaction in sarcomeric Z-disc assembly and structure, we used an integrative structural biology approach to build the first structural model of the myotilin:F-actin complex, which could serve as a blueprint for interaction of Ig-domain containing proteins with F-actin *via* two or more consecutive domains, such as the entire palladin family and filamins (18-21). This structural model suggests that binding sites for myotilin, tropomyosin and α-actinin-2 on F-actin partially overlap, which we

108 confirmed by competition assays. Furthermore, we characterized the interaction of myotilin with α-
109 actinin-2 and showed that PI(4,5)P_2 does not have a direct regulatory effect on myotilin.

110 Based on our results we propose a model in which myotilin simultaneously binds F-actin and α-actinin
111 with the concomitant displacement of tropomyosin. This renders myotilin not only a structural
112 support for Z-disc architecture, but also a co-organiser of Z-disc assembly. Furthermore, our structural
113 model of full-length myotilin provides a platform for understanding the molecular basis of disease-
114 causing mutations and their impact on structure, ligand binding and/or regulation.

115

116 Results

117 Myotilin is a conformational ensemble in solution

118 The previously performed disorder tendency analysis of full-length myotilin revealed that the N-
119 terminal region of myotilin displays characteristics of an intrinsically disordered protein (IDP) (22). The
120 meta-structure analysis, which reflects how likely a specific residue is to be located within a compact
121 3D structure, was carried out as described previously (23), and indicated a tendency for local
122 compactions in the N-terminal ID region (**Figure 1B**).

123 For characterization of full-length myotilin, we fused thioredoxin (Trx) to its N-terminus (Trx-MYOT)
124 to prevent progressive N-terminal degradation. A globular protein at the N-terminus of myotilin was
125 shown not disturb its function *in vivo,* where GST, Myc and GFP fusions have been extensively used in
126 cell biophysics experiments (13,24,25). To investigate the hydrodynamic and structural properties of
127 Trx-MYOT, we first performed size exclusion chromatography coupled to SAXS (SEC-SAXS) (**Figure**
128 **S1A**). Right-angle laser light scattering (RALLS) data collected in parallel confirmed that the elution
129 peak corresponded to a monomeric protein (**Figure S1A**). The overall molecular parameters
130 (molecular weight M_W, the radius of gyration, R_g, and maximal intermolecular distance, D_{max},) derived
131 from the resulting SAXS profile are also compatible with a monomeric species **(Figure 1C, Table S1**).
132 The featureless descent of the SAXS profile in log plot (**Figure 1C**), and the plateau in the dimensionless
133 Kratky plot (**Figure S1B**) are characteristic for the scattering of particles that are disordered and/or
134 flexible. The calculated atom-pair distance distribution functions *P*(*r*) skewed to shorter distances and
135 the D_{max} value of ~ 200 Å also suggest flexible and elongated "string like" structures (**Figure 1C, inset**).

136 The derived *ab initio* molecular envelope of Trx-MYOT displayed an elongated multi-subunit shape
137 (**Figure 1D**). To better account for the flexibility of Trx-MYOT, we employed the ensemble optimization
138 method (EOM) (26). A genetic algorithm-based selection of representative models with their
139 respective volume fractions in solution resulted in the best fit to the data with χ^2=1.01 (**Figures 1C and**
140 **1E**). Overall, the EOM-selected models tended to be more compact than those in the random pool.
141 This is visible from the shift to smaller values of D_{max} and R_g derived from the selected models
142 compared to the distribution derived from the original pool, as the most extended models were not
143 selected (**Figures 1E, S1C and S1D**). Based on this analysis, Trx-MYOT displays a tendency to occupy
144 more compact confirmations compared to a chain with random coil linkers, in line with the predicted
145 compactness (**Figure 1B**) and the disorder tendency analysis (22).

In summary, Trx-MYOT in solution displays a flexible conformational ensemble with local clusters of compactness in the intrinsically disordered regions (IDR), in addition to the structured Ig domains connected by flexible linkers.

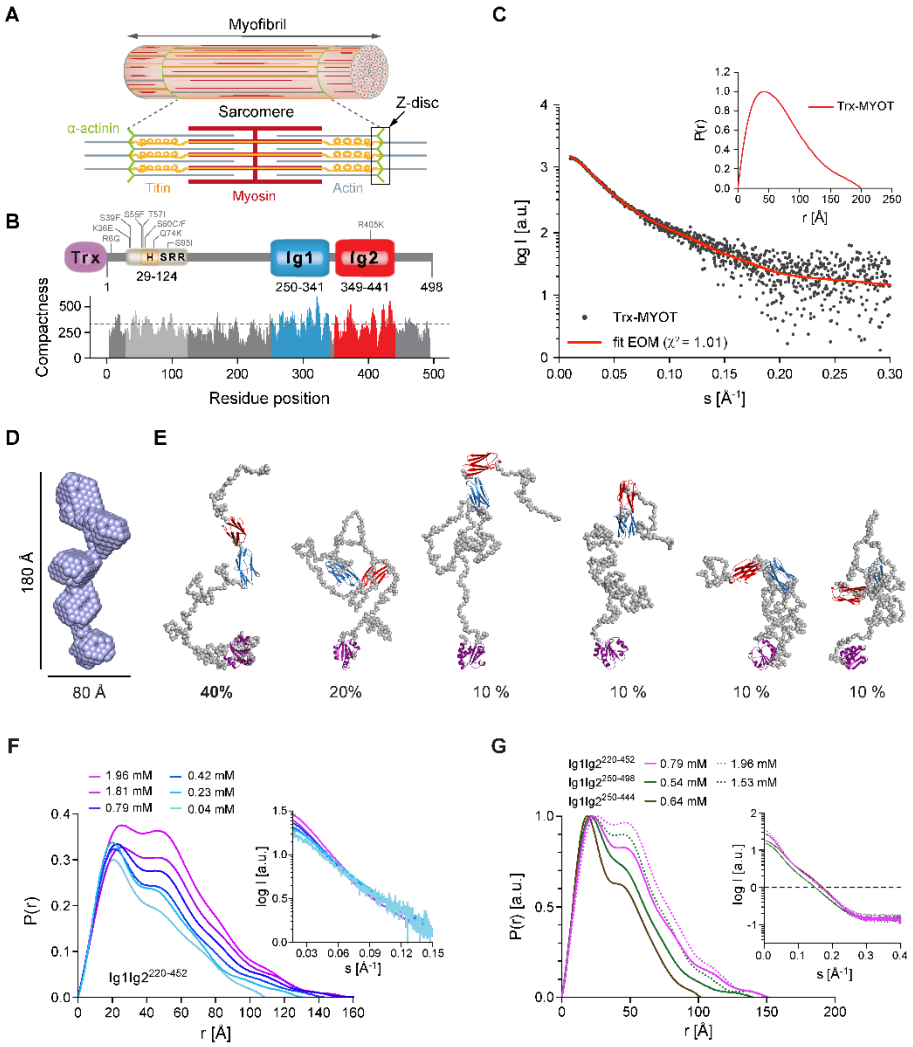

Figure 1. Myotilin displays conformational ensemble in solution. (**A**) Schematic representation of striated muscle sarcomere with its major thick (myosin-based) and thin (actin-based) filaments, titin and the Z-disc anchoring cross-linker α-actinin. Extending from one Z-disc to the next, sarcomere represents the fundamental unit of muscle contraction. (**B**) Schematic presentation of myotilin, and its predicted compactness as a function of residue position. The N-terminal part of myotilin contains the serine-rich region (SRR), which comprise hydrophobic residues stretch (H, yellow) and represents "mutational hotspot" of the protein (grey). Known disease-causing mutations are shown. C-terminal Ig domains 1 and 2, are coloured blue and red, respectively, followed by the C-terminal tail. Within this study, full-length myotilin construct fused to N-terminal thioredoxin (Trx, violet), was used. Large meta-structure derived compactness values indicate residue positions typically buried in the interior of the 3D structure, whereas small values are found for residues exposed to the solvent. Dashed line depicts the average compactness value (about 300) of the well-folded protein. Significantly smaller values (200) are found for structurally flexible proteins (23). (**C**) Experimental SAXS scattering data of Trx-MYOT, with the fit of the EOM flexible modelling. Inset, *P*(*r*) *vs. r* plot for Trx-MYOT with the D_{max}~200 Å. (**D**) SAXS-based *ab initio* molecular envelope of Trx-MYOT. Most probable model is shown. (**E**) EOM models of Trx-MYOT showing flexible and intrinsically disordered N- and C-terminal regions (grey). The selected models are presented with the percentage contribution, estimated from the final population of EOM models. (**F**) *P(r) vs. r* plot for concentration series of $Ig1Ig2^{220-452}$. Inset, respective concentration series with the corresponding SAXS profiles. (**G**) *P(r) vs. r* plot for dimeric $Ig1Ig2^{220-452}$, $Ig1Ig2^{250-498}$ and monomeric $Ig1Ig2^{220-444}$. Inset, SAXS profiles of respective constructs. In order to compare various *P(r)* functions, *P(r)* was normalized to the peak height. See also Figure S1 and Table S1.

150 ## Myotilin forms concentration-dependent dimers

151 Although myotilin was suggested to form antiparallel dimers (10) full-length myotilin was monomeric
152 under our experimental conditions. The shortest myotilin fragment with the ability to dimerize was
153 reported to include the Ig2 domain and the C-terminal tail (17). To investigate molecular determinants
154 of dimerization we used SAXS on a series of truncated constructs: Ig1Ig2$^{250-444}$ (Ig1Ig2 tandem),
155 Ig1Ig2$^{220-452}$ and Ig1Ig2$^{250-498}$.

156 We monitored the maximum scattering intensities extrapolated to zero angle (I_0) for a concentration
157 series of the Ig1Ig2$^{220-452}$ construct, and observed a concentration-dependent increase in the average
158 molecular mass of resulting particles (**Figure 1F, inset**). Accordingly, the *P*(*r*) function for Ig1Ig2$^{220-452}$
159 showed a transition from a typical distribution for an extended two-domain protein, with a significant
160 peak at approximately 25 Å and a minor at 50 Å, to a distribution with increased frequencies of the 50
161 Å peak and a new minor signal at in the region 80-100 Å (**Figure 1F**). Here, the shortest vector
162 corresponds to the distances within Ig domains, while the second and the third peaks correspond to
163 inter-domain distances within and between the subunits with concomitant increase of D_{max} value to
164 approximately 150 Å (**Figure 1F, and Table S1**). The notable increase of the D_{max} value in a
165 concentration dependent manner from 110 Å together with *P(r)* suggest an antiparallel staggered
166 dimer formed by interactions *via* Ig1 (head-to-head) or Ig2 domains (tail-to-tail), and not a parallel or
167 antiparallel dimerisation arrangement formed by interactions *via* both domains (**Figures 1F, S1E and**
168 **S1F**). While the model-derived *P(r)* also supports a staggered parallel dimer architecture, the SAXS
169 data does not since such architecture would allow polymerization hence resulting in much higher D_{max}
170 values than calculated from the experimental data (**Figures S1E and S1F**).

171 *P(r)* functions of Ig1Ig2$^{250-444}$, Ig1Ig2$^{220-452}$ and Ig1Ig2$^{250-498}$ derived from scattering data at comparable
172 concentrations showed that Ig1Ig2$^{220-452}$ and Ig1Ig2$^{250-498}$ displayed a high second peak at 50 Å, and
173 corresponding D_{max} values of approximately 150 Å (**Figure 1G, and Table S1**), whereas Ig1Ig2$^{250-444}$ did
174 not. Guinier region analysis revealed an apparent increase of R_g for the Ig1Ig2$^{220-452}$ and Ig1Ig2$^{250-498}$,
175 whereas Ig1Ig2$^{250-444}$ displayed molecular parameters of a monomeric species, comparable to those
176 observed for Ig1Ig2$^{220-452}$ at low concentrations (**Figures 1F, and Table S1**). Consequently, M_W values
177 calculated from I_0 using the Guinier approximation correspond to the expected M_W of a dimer for
178 Ig1Ig2$^{220-452}$, approaching dimer for Ig1Ig2$^{250-498}$ and of a monomer for Ig1Ig2$^{250-444}$ (**Table S1**),
179 corroborating the role of regions flanking the Ig1Ig2.

180 R405 is mutated in muscular dystrophy, and was suggested to be responsible for defective homo-
181 dimerization of myotilin (27). We therefore assessed the dimerisation propensity of Ig1Ig2$^{220-452\ R405K}$
182 mutant using SAXS. Comparative analysis of SAXS data and derived molecular parameters (D_{max}, R_g,
183 *P(r)*, M_W) revealed that the conserved R405K mutation which preserves the positive charge does not
184 impair dimer formation *in vitro,* (**Figures S1G and Table S1**), in contrast to previously reported
185 defective homo-dimerisation observed by immunoprecipitation and yeast two hybrid screens (27).

186 Our results together with published data on myotilin dimerization collectively show that: (i) N- and C-
187 terminal regions flanking the Ig1Ig2 domains contribute to dimer stabilisation in solution; (ii) the fully
188 dimeric form is observed only at high protein concentrations (> 1.0 mM), suggesting a weak
189 association constant, explaining why only monomers of Trx-MYOT were observed in our SEC-SAXS
190 experiments; (iii) tail-to-tail dimerisation reconciles both SAXS analysis and proposed mode of
191 incorporation in the Z-disc, ochestered by interactions with filamin C and α-actinin-2 (10).

192

193 ## Tandem Ig-domains of myotilin together with contiguous regions are required for high
194 affinity binding to F-actin

195 To characterise myotilin:F-actin interaction and to elucidate the suggested role of segments flanking
196 Ig1Ig2 (10,17), we determined the binding affinity of full-length Trx-MYOT, and a series of truncated
197 constructs, using F-actin co-sedimentation assays (**Figure 2A**).

198 In the initial experiments (using conditions B1, for details, see Materials and Methods) with single Ig
199 domains ($Ig1^{250-344}$ and $Ig2^{349-459}$), and their tandem ($Ig1Ig2^{250-444}$), neither Ig1, nor Ig2 alone displayed
200 significant binding to F-actin, while $Ig1Ig2^{250-444}$ bound to F-actin with K_d = 9.2 ± 1.0 µM (**Figures 2A and**
201 **S2A**). When the same experimental conditions were used for Trx-MYOT, its self-pelleting was
202 observed making interpretation of the data difficult. To reduce the fraction of self-pelleted Trx-MYOT,
203 we optimized the conditions for the co-sedimentation assays using a differential scanning fluorimetry
204 (DSF)-based pH-screen (**Figure S2C**). We found that a slightly acidic pH, i.e. an adjustment of the assay
205 buffer from pH 7.4 (in conditions B1) to pH 6.8 (conditions B2, for details, see Materials and Methods)
206 rendered Trx-MYOT more stable as well as more soluble. To assess the effect of pH (6.8), affinity of
207 $Ig1Ig2^{250-444}$ to F-actin was determined using the conditions B2, too. The observed apparent K_d (12.9 ±
208 1.5 µM) was in good agreement with the affinity measured in the B1 conditions (K_d = 9.2 ± 1.0 µM)
209 (**Figures 2A and S2B**, left panel), suggesting that diverse conditions used do not have a major effect
210 on the myotilin affinity to F-actin.

211 The apparent K_d of Trx-MYOT for F-actin in conditions B2 is 0.29 ± 0.06 µM (**Figures 2A and S2B**, right
212 panel), indicating relatively strong binding compared to other F-actin binding proteins of the palladin
213 family. For instance, the affinity of full-length palladin to F-actin was reported to be 2.1 ± 0.5 µM (18).
214 To further delineate the role of regions flanking Ig1Ig2, $Ig1Ig2^{185-454}$, $Ig1Ig2^{250-498}$, and $Ig1Ig2^{185-498}$ were
215 assayed for F-actin binding (**Figures 2A and S2B**). All constructs bound to F-actin with similar affinity
216 (K_d = 3.0 ± 0.6 µM, 1.2 ± 0.2 µM, and 2.0 ± 0.4 µM for $Ig1Ig2^{185-454}$, $Ig1Ig2^{250-498}$, and $Ig1Ig2^{185-498}$,
217 respectively), and thus significantly stronger than the $Ig1Ig2^{250-444}$ encompassing only the two Ig
218 domains (**Figures 2A and S2B**).

219 The surface electrostatic potential of the tandem Ig1Ig2 domains displays positive clusters on one face
220 of the domains ('BED' β-sheet) and in general a more pronounced basic character of Ig2 in contrast to
221 Ig1 (**Figure 2B**). Positive clusters have also been observed in several other F-actin binding proteins,
222 including palladin (28), suggesting an electrostatically driven interaction. To investigate the influence
223 of ionic strength on the affinity we performed co-sedimentation assays with increasing NaCl
224 concentrations. As shown in **Figure 2C**, higher salt concentrations reduced the ability of myotilin to
225 co-sediment with F-actin.

226 To further corroborate the electrostatic nature of the interaction, we gradually neutralized the
227 positive charge by mutating the basic residues of the Ig2 domain to Ala in the construct $Ig1Ig2^{250-444}$.
228 While mutations of Q356A, K411A and K367A did not significantly affect binding to F-actin compared
229 to the wild-type, single mutations K358A, K359A, and K354A had a negative effect, which was
230 remarkably potentiated in the double K354/359A mutant, and even more in the K354/358/359A triple
231 mutant (**Figure 2D**). The latter mutant showed a 70% reduction in binding to F-actin, suggesting that
232 this basic patch in Ig2 plays an important role in F-actin binding (**Figure 2B and 2D**).

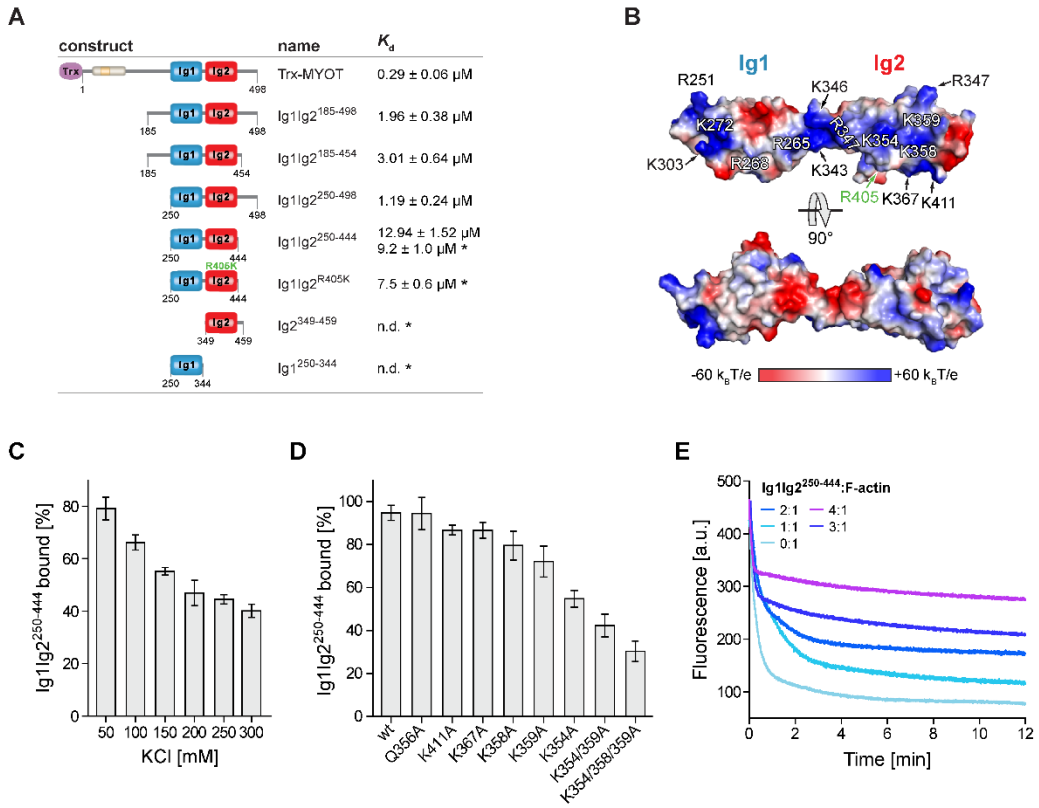

Figure 2. Myotilin influences F-actin dynamics by binding *via* its Ig domains and disordered flanking regions. (**A**) Summarized results of the actin co-sedimentation assays. The asterisk denotes values obtained in assays performed under B1 conditions (for details see Material and Methods). (**B**) Surface electrostatic potential mapped on the Ig1Ig2 structural model (22). Surfaces are coloured on a red-white-blue gradient, as calculated by Adaptive Poisson-Boltzmann Solver (29). Residues forming a basic patch (blue) on both Ig domains are labelled. The residue (R405) involved in muscular dystrophy-causing mutation R405K is shown in green (27). (**C**) Binding of Ig1Ig2$^{250-444}$ to F-actin at increasing salt conditions. Graph data are presented as a percentage of theoretical total binding (100 %) corresponding to the total amount of protein (8 μM) used in each experiment. Data represent mean values ± SEM of three independent experiments. The mean binding of Ig1Ig2$^{250-444}$ to F-actin in 50 mM KCl was significantly different to the means for all other tested concentrations of KCl. Significance was assessed using one-way ANOVA with Holm-Sidak test, $p < 0.001$ for salt concentration of 50 mM vs. all other tested concentrations. (**D**) Binding of Ig1Ig2$^{250-444}$ and its mutant versions to F-actin. Graph data are presented as in (**C**). Data represent mean values ± SEM of three independent experiments. The mean binding to F-actin of all mutants except Q356A, K411A and K367A were significantly different from the means of WT Ig1Ig2$^{250-444}$. Significance was assessed using one-way ANOVA with Holm-Sidak test, $p < 0.01$ for WT vs. K358A and $p < 0.001$ for WT vs. all other mutants. (**E**) Effects of Ig1Ig2$^{250-444}$ on F-actin depolymerization. Actin filaments were depolymerized in the presence or absence of Ig1Ig2$^{250-444}$ at molar ratios indicated in the figure. See also Figure S2.

233 The muscular dystrophy-causing mutant R405K (Ig1Ig2^{R405K}) (27) was also tested, but did not show any
234 notable difference in F-actin affinity with respect to the wild-type (Figures 2A and S2A), which agrees
235 with its lateral location with respect to the identified positively charged patch involved in F-actin
236 binding. Furthermore, the mutation retains the positive charge at this position (Figure 2B).

237 Since binding data is available for other actin-binding Ig domains, e.g. for Ig domains of palladin and
238 filamin A (19), we conducted a comparative structural analysis of the actin-binding Ig domains of
239 myotilin, the Ig3 domain of palladin, and Ig10 of filamin A, which revealed charged residues positioned
240 on the same face in all analysed Ig domains (Figures S2D). Notably, these residues coincide with those
241 indicated by co-evolution analysis (30) as potentially functional sites (Figure S2D, lower panel).
242 Specifically, lysine residues K1008, K1011 and K1044 on palladin Ig3 domain were shown to be

243 essential for F-actin binding (28). Equivalent residues are also present in myotilin (**Figure S2D**, upper
244 panel), and form a basic patch, which extends from one Ig domain to the other (**Figure 2B**).

245 Finally, we biochemically characterized the previously observed myotilin binding to (monomeric) G-
246 actin (17) using a constitutively monomeric mutant of actin, DVD-actin (31). We employed microscale
247 thermophoresis (MST) with various myotilin tandem or isolated Ig domain constructs. The affinity of
248 myotilin constructs to non-polymerizable DVD-actin was two orders of magnitude lower than that to
249 F-actin (**Figures S2E and S2F**). The highest affinity displayed by construct Ig1Ig2$^{185-454}$ indicates that,
250 similar to F-actin, the Ig-domain-flanking regions could be involved in modulating actin dynamics.

251 We hence performed depolymerization assays, to obtain further insight into the role of myotilin in
252 actin dynamics. As also observed for the full-length myotilin (10), addition of Ig1Ig2$^{250-444}$ reduced F-
253 actin depolymerization rate in a concentration-dependent manner (**Figure 2E**), suggesting that the
254 tandem Ig domains play the critical role in actin binding.

255 In summary, our results reveal that myotilin has a role in stabilization of actin filaments and actin
256 dynamics, where the tandem Ig domains play the central role and that both the N- and C-terminal
257 neighbouring regions further enhance affinity and stabilise the myotilin:F-actin interaction (**Figure**
258 **2A**).

259

260 ## Integrative structural model of the myotilin:F-actin complex

261 To validate and identify potential new contacts with Ig domains and with their contiguous regions, as
262 implied from the binding and mutational data (**Figure 2A and 2D**), we performed XL-MS experiments
263 on Ig1Ig2$^{250-444}$, Ig1Ig2$^{185-454}$ and Ig1Ig2$^{185-498}$ bound to F-actin (**Figures S3A-S3C**). As expected, specific
264 cross-links involving both Ig1 and Ig2 domains as well as their N- and C-terminal flanking regions
265 (**Figures 3A and Table S2**) were found. While only one cross-link was detected between the Ig1 domain
266 and F-actin (K303 on Ig1 and D27 on actin), there were several cross-links between the Ig2 domain
267 and F-actin. This is in line with its higher affinity and the charged nature of this interaction (**Figures**
268 **2B, 2D, and S2A**), leading to cross-links of basic lysine residues on Ig2 domain with the acidic residues
269 located in subdomain 1 of actin. Of the Ig2 domain residues cross-linked to F-actin, we also found K354
270 involved in the interaction using mutagenesis and co-sedimentation assays (**Figures 2D and 3A**).
271 Furthermore, the cross-links between acidic myotilin residues (D236, D239 and D241) and basic K328
272 and K330 on actin (**Figure 3A and Table S2**) map to the region preceding myotilin Ig1 in constructs
273 Ig1Ig2$^{185-454}$ and Ig1Ig2$^{185-498}$. The latter construct yielded additional cross-links between positively
274 charged K452, K462 and K474 mapping to the region C-terminal to Ig2, and negatively charged
275 residues E336, D27 and D26 on actin (**Figure 3A and Table S2**).

276 To construct an integrative molecular model of the myotilin:F-actin complex, we combined our
277 structural model of Trx-MYOT (**Figure 1E**) and experimental data derived from *in vitro* mutational
278 analysis and XL-MS, which we used as experimental distance restraints that guided the
279 macromolecular docking using Haddock 2.2 (32) (for details see Material and Methods). In this model
280 the tandem Ig domains land on the subdomains 1 of the adjacent actin subunits, with the flexible N-
281 and C-terminal regions extending to the binding sites on neighbouring actin subunits as suggested by
282 XL-MS data (**Figures 3B**).

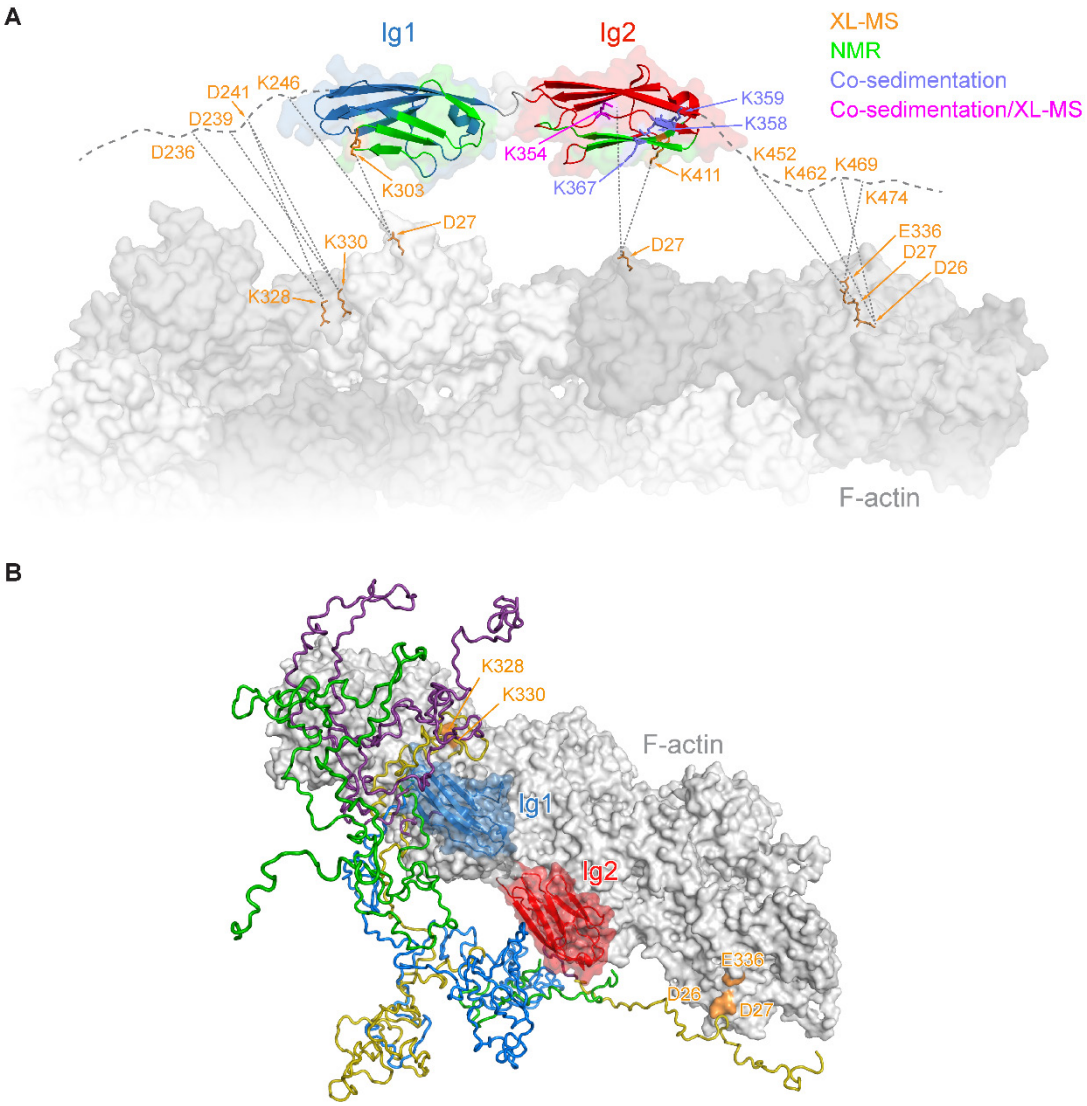

Figure 3. Integrative structural model of myotilin:F-actin complex. (**A**) Summary of experimental data on myotilin:F-actin complex, obtained from XL-MS (orange), co-sedimentation/mutagenesis analysis (medium slate blue), and NMR (green). K354 was found to be involved in the interaction by both XL-MS and co-sedimentation/mutagenesis analysis (magenta). Thick, grey dashed lines represent N- and C-terminal flanking regions of myotilin Ig domains. Selected residues found in cross-links between actin and myotilin are shown in orange. (**B**) Model of the full-length myotilin bound to F-actin. Ig domains of myotilin were docked on F-actin and combined with flexible (not docked) models of N- and C-terminal parts of the protein from EOM analysis of Trx-MYOT (**Figure 1E**). The four most populated conformations of N- and C-terminal parts are shown in distinct colours. Selected residues of actin found in cross-links with myotilin are shown in orange. See also **Figure S3 and Table S2**.

283 NMR was subsequently used to validate the structural model of myotilin:F-actin complex. NMR
284 spectra of the isolated ^{15}N-labelled Ig1 and Ig2 domains showed similar characteristics to those
285 available in the BMRB databank (Ig1: 7113; Ig2: 16370) (33), and hence *de novo* assignment was not
286 required in order to obtain a subset of assigned peaks. Construct Ig1Ig2$^{250-444}$ also showed a similar
287 peak pattern, allowing the use of assignments of the single domains to obtain a partial assignment of
288 this tandem construct. In the initial HSQC experiments, ^{15}N-labelled Ig1$^{250-344}$ was titrated with F-actin,
289 which induced a reduction of the signal intensities (**Figure S3D**). Measurements of the ^{15}N-labelled Ig2
290 domain (Ig2$^{349-459}$) showed a stronger reduction in signal intensity upon addition of F-actin compared
291 to those carried out with the Ig1 domain (**Figure S3D**) indicating stronger binding of Ig2 to F-actin.

292 Further experiments with ^{15}N-labelled Ig1Ig2$^{250-444}$ showed a shift pattern upon addition of F-actin,
293 where the regions with significant HSQC shifts are: 257-270, 296-309, 363-374 and 405-413 (**Figure**
294 **S3E and S3F**) with segment 301-306 unfortunately not being represented due to low signal intensity
295 (33). These regions map to the 'BED' β-sheet of both Ig domains and additionally to the β-strand A' in
296 Ig1, and are in agreement with the interaction sites mapped by binding, mutational and XL-MS data
297 (**Figure 2A, 2D and 3A**).

298

299 ## Myotilin competes with tropomyosin and α-actinin-2 for the binding sites on F-actin

300 The actin residues identified in the myotilin:F-actin interaction by XL-MS include K328, K330 and D26,
301 D27 and E336 (**Figures 3A and 3B**). Interestingly, K328, together with neighbouring K326, form the
302 major interaction site for tropomyosin on F-actin (34), implying that myotilin and tropomyosin could
303 compete for binding to F-actin. We therefore created a structural model of myotilin bound to F-actin
304 in the presence of tropomyosin (**Figure 4A**). In this model, two Ig domains of myotilin only marginally
305 overlap with tropomyosin bound to F-actin. However, their N- and C-terminal flanking regions found
306 by XL-MS analysis to interact with actin residues (D26, D27, K326, K328, and E336), map to or close to
307 the tropomyosin binding site (**Figure 4A**), suggesting that they might interfere with F-
308 actin:tropomyosin binding.

309 To test this hypothesis, we performed competition co-sedimentation assays where F-actin was
310 incubated with increasing concentrations of Trx-MYOT, either before or after adding a fixed amount
311 of the striated muscle isoform of human tropomyosin (Tpm1.1). The amount of tropomyosin bound
312 to F-actin decreased with increasing concentrations of Trx-MYOT (**Figures 4B and S4A**), uncovering
313 that myotilin competes with tropomyosin for F-actin binding and displaces tropomyosin from F-actin.

314 In the myofibrillar Z-disc, myotilin associates with the striated muscle-specific isoform α-actinin-2
315 (9,11), the major Z-disc protein. As the stress-fibre-associated tropomyosin isoforms were shown to
316 compete with non-muscle α-actinin-1 and α-actinin-4 for F-actin binding (35,36), we examined
317 whether α-actinin-2 is also able to compete with tropomyosin for F-actin. We used the constitutively
318 open variant of α-actinin-2, in which mutations abrogating binding of EF34 to the α-actinin-2 "neck"
319 region were introduced (ACTN2-NEECK, **Figure 4C**) to resemble the Z-disc bound conformation of α-
320 actinin-2 (7). We performed competition co-sedimentation assays, in which α-actinin-2 was incubated
321 at increasing concentrations with F-actin before the addition of tropomyosin. As expected, binding of
322 α-actinin-2 to F-actin prevented tropomyosin-F-actin binding in a concentration dependent manner
323 (**Figures 4D and S4B**).

324 Comparative structural analysis of the myotilin:F-actin:tropomyosin model (**Figure 4A**) and the cryo-
325 EM structures of F-actin decorated with the actin binding domain (ABD) of α-actinin-2, spectrin or
326 filamin (37-39), showed that binding sites of myotilin, tropomyosin and α-actinin-2 on F-actin overlap
327 (**Figure S4C**). Furthermore, comparison of binding affinities of myotilin, tropomyosin and α-actinin-2
328 to F-actin (35,40-43) together with our competition assays (**Figures 4B and 4D**), indicate that myotilin
329 could displace both tropomyosin and α-actinin-2 from F-actin, suggesting a novel role of myotilin as a
330 regulator of access of tropomyosin and other actin-binding proteins to F-actin in the Z-disc.

331

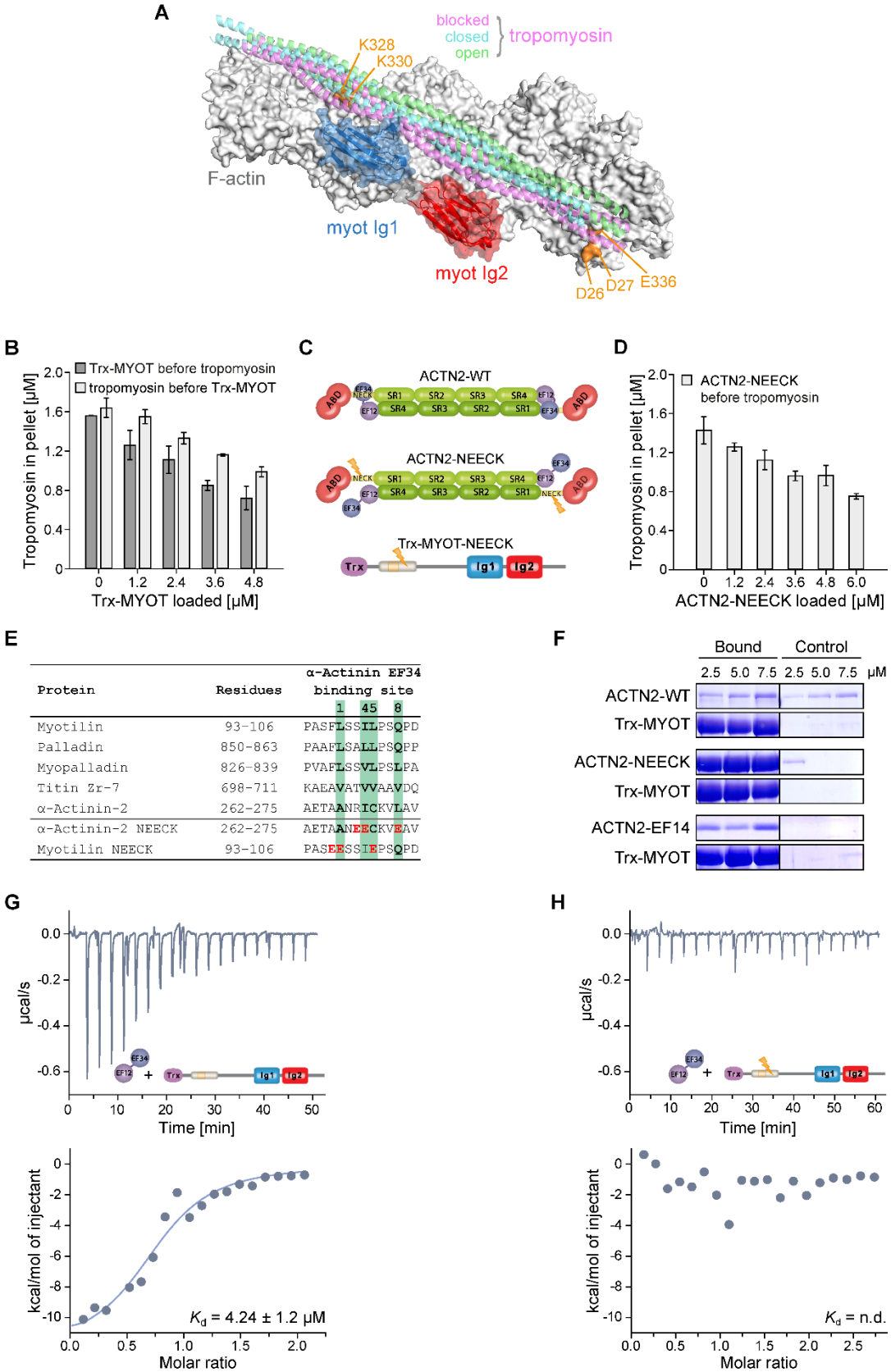
A
blocked
closed
open
tropomyosin
K328
K330
F-actin
myot Ig1
myot Ig2
D26
D27
E336
B
Trx-MYOT before tropomyosin
tropomyosin before Trx-MYOT
Tropomyosin in pellet [μM]
Trx-MYOT loaded [μM]
C
ACTN2-WT
ACTN2-NEECK
Trx-MYOT-NEECK
D
ACTN2-NEECK before tropomyosin
Tropomyosin in pellet [μM]
ACTN2-NEECK loaded [μM]
E
Protein
Residues
α-Actinin EF34 binding site
Myotilin 93-106 PASFLSSILPSQPD
Palladin 850-863 PAAFLSALLPSQPP
Myopalladin 826-839 PVAFLSSVLPSLPA
Titin Zr-7 698-711 KAEAVATVVAAVDQ
α-Actinin-2 262-275 AETAANRICKVLAV
α-Actinin-2 NEECK 262-275 AETAANEECKVEAV
Myotilin NEECK 93-106 PASEESSIEPSQPD
F
Bound
Control
2.5 5.0 7.5 2.5 5.0 7.5 μM
ACTN2-WT
Trx-MYOT
ACTN2-NEECK
Trx-MYOT
ACTN2-EF14
Trx-MYOT
G
μcal/s
Time [min]
kcal/mol of injectant
Molar ratio
K_d = 4.24 ± 1.2 μM
H
μcal/s
Time [min]
kcal/mol of injectant
Molar ratio
K_d = n.d.

Figure 4. Myotilin regulates binding of tropomyosin to F-actin and interacts with α-actinin-2. (**A**) Model of tandem Ig domains of myotilin bound to F-actin superimposed with the cryo-EM structures of cardiac tropomyosin bound to F-actin in the blocked (magenta ribbons, PDB: 5NOG), closed (cyan ribbons, PDB: 5NOL), and open (green ribbons, PDB: 5NOJ) structural states (44). Residues of actin found in cross-links with N- and C-terminal regions flanking myotilin Ig domains are shown in orange (see Figure 3A). (**B**) Effects of myotilin on tropomyosin:F-actin interaction. Myotilin (Trx-MYOT) at increasing concentrations was added to F-actin before (Trx-MYOT before tropomyosin) or after (tropomyosin before Trx-MYOT) incubation of F-actin with the fixed amount of tropomyosin. Mean values (± SEM) of three independent experiments are shown. For "Trx-MYOT before tropomyosin" the mean binding of tropomyosin to F-actin at all concentrations of Trx-MYOT was significantly different from the means in the absence of Trx-MYOT. Significance was assessed using one-way ANOVA with Holm-Sidak test, $p < 0.01$ for 0 vs. 1.2 µM Trx-MYOT and $p < 0.001$ for 0 vs. all other concentrations of Trx-MYOT. For "Tropomyosin before Trx-MYOT" the mean binding of tropomyosin to F-actin at all concentrations of Trx-MYOT, except for 1.2 µM Trx-MYOT, was significantly different from the means in the absence of Trx-MYOT. Significance was assessed using one-way ANOVA with Holm-Sidak test, $p < 0.05$ for 0 vs. 2.4 µM Trx-MYOT, $p < 0.01$ for 0 vs. 3.6 µM Trx-MYOT and $p < 0.001$ for 0 vs. 4.8 µM Trx-MYOT. (**C**) Schematic presentation of the wild-type α-actinin-2 (ACTN2-WT), its constitutively open mutant (ACTN2-NEECK), and mutant of Trx-MYOT (Trx-MYOT-NEECK), possessing mutations resembling those in the ACTN2-NEECK (see Figure 4E). Lightning bolt depicts position of mutations. (**D**) Effects of myotilin on α-actinin:F-actin interaction. ACTN2-NEECK was added to F-actin at increasing concentrations before (ACTN2-NEECK before tropomyosin) incubation of F-actin with the fixed amount of tropomyosin. Mean values (± SEM) of three independent experiments are shown. The mean binding of tropomyosin to F-actin at all concentrations of ACTN2-NEECK was significantly different from the means in its absence. Significance was assessed using one-way ANOVA with Holm-Sidak test, $p < 0.05$ for 0 vs. 1.2 µM ACTN2-NEECK, $p < 0.01$ 0 vs. 2.4 µM ACTN2-NEECK, and $p < 0.001$ for 0 vs. all other concentrations of ACTN2-NEECK. (**E**) Sequence alignment of proteins and their residues involved in binding to α-actinin EF34. Residues of the CaM-binding motif 1-4-5-8 are shown in bold and boxed in green. Residues mutated in α-actinin-2 NEECK and myotilin NEECK are shown in red. (**F**) Binding of myotilin to α-actinin. ACTN2-WT, ACTN2-NEECK, for details see (**C** and **E**), and α-actinin-2 EF14 (ACTN2-EF14) were subjected at increasing concentrations to pull-down assay with (bound) or without (control) Trx-MYOT. (**G** and **H**) Results of ITC experiments quantifying the interaction between (**G**), Trx-MYOT, or (**H**) its mutant (Trx-MYOT-NEECK), for details see (**C** and **E**) and ACTN2-EF14. n.d., not determined. See also Figure S4.

Myotilin binds α-actinin-2 using the same pseudoligand regulatory mechanism as titin

α-Actinin-2 interacts with titin as well as with pallading family of proteins *via* its C-terminal EF-hands (EF34) of the calmodulin-like domain (CAMD) (45-47). The interaction between α-actinin-2 and titin binding motifs, the Z-repeats, has been well characterised (7,8,45), and was shown to be regulated by an intramolecular pseudoligand mechanism, in which a titin Z-repeat-like sequence ("neck", which contains the 1-4-5-8 binding motif) connecting the ABD and the first spectrin repeat of α-actinin-2, interacts with EF34 of the juxtaposed CAMD (Figure 4C). In this closed conformation, EF34 are not available for interactions to titin Z-repeats unless $PI(4,5)P_2$ catalyzes conformational switch to the open confirmation through their release from the "neck", and hence activating titin binding (7).

The interaction between α-actinin-2 and myotilin maps to the N-terminal part of myotilin, which also contains the conserved 1-4-5-8 motif (residues 95-106, Figures 4C and 4E) similar to palladin and myopalladin (47). This was suggested by NMR experiments where a myotilin peptide containing the binding motif (Figure 4E) was titrated to EF34 (47).

To characterize the interaction of myotilin with α-actinin-2 with full-length proteins we firstly performed pull-down assays using either wild-type α-actinin-2 (ACTN2-WT), its constitutively open mutant ACTN2-NEECK, or CAMD encoding all four EF-hands of α-actinin-2 (ACTN2-EF14), with Trx-MYOT (Figures 4C and 4E). We observed myotilin binding to ACTN2-NEECK and ACTN2-EF14, but not to ACTN2-WT (Figure 4F) indicating that opening of α-actinin-2 is necessary for its interaction with myotilin, as was also revealed for titin (7).

To validate the binding site between α-actinin-2 and myotilin (Figures 4C and 4E), we next performed ITC experiments with ACTN2-EF14, Trx-MYOT and its mutant variant (Trx-MYOT-NEECK), where mutations resembling those in ACTN2-NEECK were introduced in the binding motif to disrupt the

354 interaction. Indeed, the affinity of Trx-MYOT to α-actinin-2 was found to be in μM range (K_d = 4.2 ±
355 1.2 μM, **Figure 4G**), whereas no binding of Trx-MYOT-NEECK to ACTN2-EF14 was observed (**Figure 4H**).

356 Altogether our data reveal that myotilin, which contains the conserved α-actinin-2 binding motif,
357 binds to the open confirmation of α-actinin-2 *via* pseudoligand regulatory mechanism.

358

359 Interaction of myotilin with F-actin is not regulated by PI(4,5)P_2

360 The Ig3 domain of palladin is the minimum fragment necessary for binding to F-actin (18,28).
361 Furthermore, Ig3 interacts with the head group of PI(4,5)P_2 with a moderate affinity (K_d = 17 μM)
362 leading to a decreased F-actin cross-linking and polymerization activity (48). Myotilin binding to α-
363 actinin-2 uses the same PI(4,5)P_2 mechanism as titin, while its F-actin binding is similar to that of
364 palladin. Therefore, we investigated whether myotilin binds PI(4,5)P_2 as well, using a liposome co-
365 sedimentation assay (48). The amount of protein bound to liposomes was examined by using a
366 constant concentration of Ig1Ig2$^{250-444}$, while varying the PI(4,5)P_2 concentration (0-20%) in 1-
367 palmitoyl-2-oleoyl-sn-glycero-3-phosphocholine (POPC) vesicles. As positive controls, double C2-like
368 domain-containing protein beta (Doc2b), a known sensor of PI(4,5)P_2 (49), and the Ig3 domain of
369 palladin were used (**Figures S4D and S4E**). Both proteins, but not myotilin Ig1Ig2$^{250-444}$ co-pelleted with
370 PI(4,5)P_2-POPC vesicles in a PI(4,5)P_2 concentration dependent manner (**Figures S4D and S4E**)
371 indicating that myotilin does not interact with PI(4,5)P_2. This observation was further corroborated by
372 structure-based sequence analysis, which showed that residues important for binding of PI(4,5)P_2 to
373 palladin (48) are not present in the Ig2 domain of myotilin (**Figure S4F**). Therefore, the myotilin
374 interaction with F-actin is most likely not regulated by PI(4,5)P_2.

375

376 Binding to F-actin affects myotilin mobility and dynamics in cells

377 To assess whether actin-binding affects the cellular dynamics of myotilin, we expressed N-terminal
378 EGFP fusion of myotilin, or its mutants that showed impaired F-actin binding activity *in vitro* (K354A,
379 K359A, K354/359A, K354/358/359A), in differentiating C2C12 mouse myotubes. After seven days of
380 differentiation, all of the tested mutants and the wild-type myotilin showed a similar distribution and
381 localized to Z-discs (**Figure 5A, panel "pre-bleaching"**), suggesting that similarly to EGFP, N-terminal
382 Trx-tag used for *in vitro* studies does not perturb myotilin function. Fluorescence recovery after
383 photobleaching (FRAP) was performed to compare the mobility and dynamics of the mutant variants
384 with wild-type myotilin (**Figure 5A**). Wild-type myotilin showed rapid dynamics with 80% fluorescence
385 recovery after 300 s (median halftime $t_{1/2}$ of 72.4 s) (**Figure 5B**), which is in excellent agreement with
386 previously published reports (50,51). While the single mutant K359A only showed slight, non-
387 significant changes ($t_{1/2}$ 64.1 s), K354A showed significantly faster recovery with $t_{1/2}$ of 48.2 s (**Figures**
388 **5B and 5C**). Protein dynamics further increased proportionally to the number of mutations in double
389 ($t_{1/2}$ 35.5 s) and triple ($t_{1/2}$ 32.3 s) mutants (**Figures 5B and 5C**). The differences in recovery times are
390 evident by comparing the fluorescence signals in **Figure 5A**: the wild-type and K359A myotilin hardly
391 showed any recovery after 5 or even 20 s, indicating relatively slow dissociation and high affinity, but
392 a clear signal can be seen for the other three mutants with reduced actin binding strength. At the
393 same time, the mobile fraction of the mutants increased correspondingly (**Figure 5D**).

394 These results show that mutant myotilin variants with decreased binding to F-actin *in vitro* have
395 significantly altered dynamics in the sarcomeric Z-disc, indicating that binding to F-actin stabilizes
396 myotilin in the sarcomere.

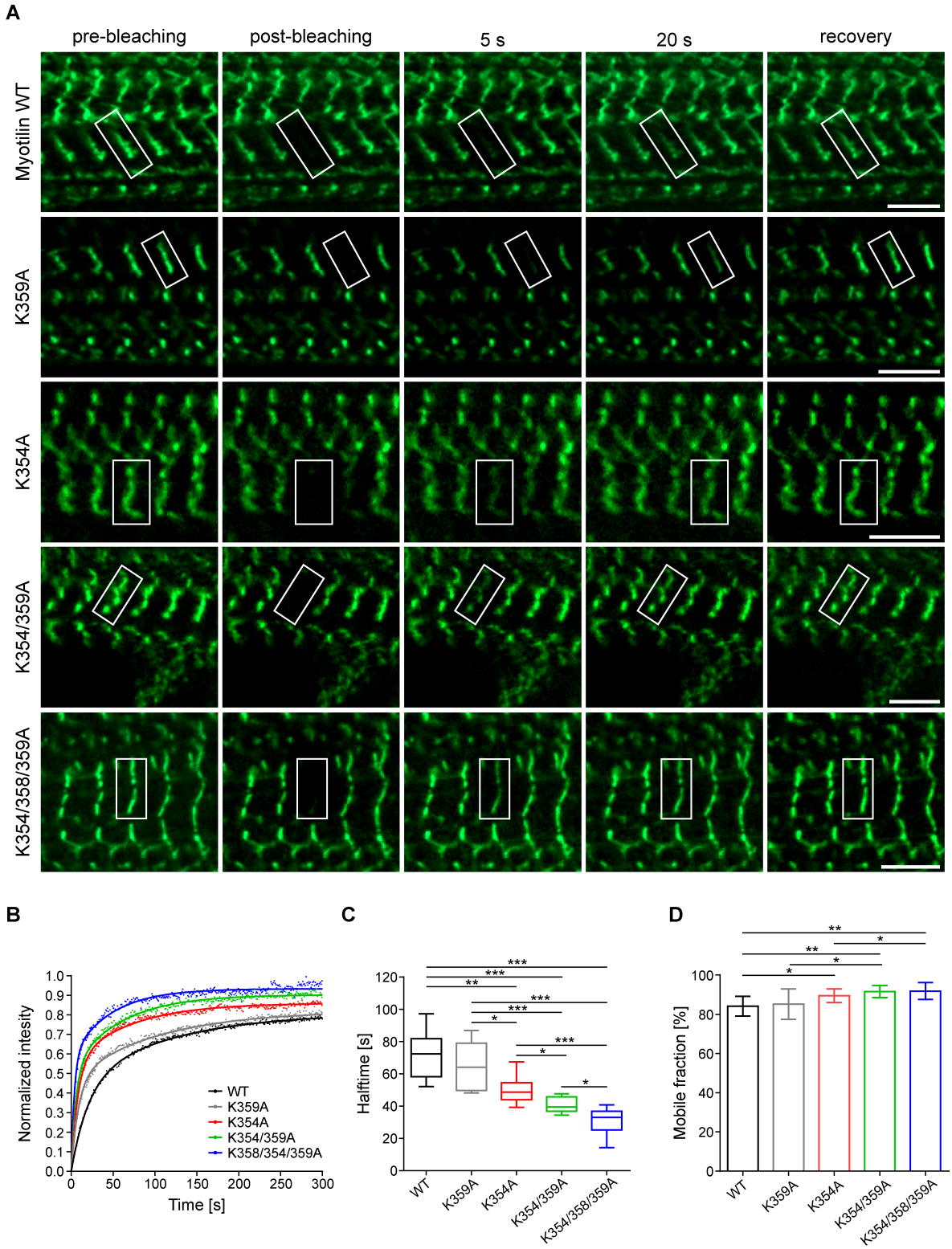

Figure 5. Binding of myotilin with F-actin affects its mobility and dynamics. (**A**) FRAP analysis of the dynamics of myotilin and its mutant variants in Z-discs. Localization of EGFP-fusion proteins of wild-type (WT) myotilin and its variants with the indicated mutations in Ig2 before bleaching (pre-bleaching), directly after bleaching (post-bleaching) and after the indicated time points after bleaching. White rectangles show regions of interest (ROI), used for bleaching during FRAP experiments. Scale bars, 5 µm. (**B**) Representative FRAP recovery curves of the myotilin variants. (**C**) Halftimes of myotilin mutants compared to wild-type myotilin (WT). Quantification of data from FRAP studies shown in (**A** and **B**). Statistical data are depicted in box and whisker plots. Calculated median halftimes are shown as a line surrounded by a box, representing the interquartile range comprising the median ± 25% of the data. Whiskers extend at most two standard deviations from the median. (**D**) Mobile fractions of mutants compared to wild-type myotilin. Graph reports mean ± SEM, n = 8 myotubes for each variant. 1-3 Z-discs were bleached per myotube. Significance was assessed using 2-tailed Student's t-test, *p < 0.1, **p < 0.05 and ***p < 0.01.

397

398 # Discussion

399 Biochemical and structural analysis of myotilin and its interactions presented in this study provide a
400 basis for the mechanistic understanding of its structural role in the sarcomeric Z-disc as a protein-
401 protein interaction platform, and inferring its role in orchestration of Z-disc assembly and regulation
402 of sarcomere biogenesis as an distinctive novel function of myotilin.

403 Our studies hint on Ig2 as the central F-actin interaction region, predominantly via electrostatic
404 interactions. In addition they indicate that tandem Ig1Ig2 is the minimal functional F-actin-binding
405 module, which the N- and C-terminal flanking regions further enhance binding affinity and thus
406 contribute to complex stability. This is supported by a body of evidence: i) positively charged patches
407 are on the same surface on both Ig domains, ii) XL-MS maps specific cross-links between F-actin and
408 Ig1, Ig2 as well as the flanking regions, iii) the flanking regions enhance binding to F-actin, iv) NMR
409 substantiated the interaction sites to map to the same face on both Ig domains, v) binding of tandem
410 Ig1Ig2 to F-actin stabilizes F-actin and prevents its depolymerization. The latter may be explained by
411 binding of each Ig domain to one actin subunit, allowing the tandem Ig1Ig2 to bridge two actin
412 subunits and thus act as a vertical cross-linker. The importance of tandem Ig-domains for interaction
413 with F-actin was also observed for palladin where Ig3Ig4 tandem displayed enhanced binding in
414 comparison to Ig3 alone (18). In addition, our FRAP experiments highlight the importance of the
415 positively charged patch in Ig2 for binding. Proteins with charge-neutralizing mutations in Ig2
416 displayed increased mobile fractions and shorter fluorescence recovery times in differentiated C2C12
417 cells, indicating reduced binding affinity.

418 von Nandelstadh et al (2015) previously suggested Ig1Ig2 tandem to be important for optimal
419 interaction with F-actin and showed that the size of myotilin constructs correlates with binding
420 efficiency with longer fragments binding better to F-actin (17). However, a detailed interaction map
421 and molecular mechanism of the binding was not known. Based on our findings we generated the first
422 molecular model of F-actin decorated by tandem Ig domains, which together with our quantitative
423 binding assays allowed us to propose a mechanism for myotilin:F-actin assembly. In the unbound
424 state, myotilin Ig domains are flexible, tending towards a semi-extended orientation which allows
425 conformational plasticity as part of the binding-partner recognition mechanism. In the initial step of
426 the interaction with F-actin, the positively charged region on myotilin Ig2 as the predominant binder,
427 attaches to the negatively charged subdomain 1 of actin. The subsequent Ig1:F-actin interaction
428 enables a transition to complete extension and consequently stabilization of both Ig domains and the
429 flanking regions on F-actin.

430 Although palladin and myotilin are closely related, and the interaction with F-actin is in both cases
431 mediated by a conserved mechanism involving basic charged clusters in the Ig-domains, they seem to
432 differ fundamentally in the precise geometry and stoichiometry of the complexes formed. Palladin
433 binds actin *via* two basic clusters situated on two sides of a single Ig-domain (28), allowing for cross-
434 linking two actin filaments with a single palladin molecule. By contrast, a single myotilin molecule
435 harbours only one high affinity binding site. Therefore, a dimerisation is required to enable F-actin
436 cross-linking. Furthermore, the contribution of Ig-domain-flanking regions to F-actin binding may
437 allow for regulation by post-translational mechanisms (PTMs) (4,5).

438 Since the interaction of most actin-binding proteins with F-actin may either be regulated by certain
439 compounds or modulated by other proteins, it is essential to contemplate the precise situation in the
440 cell. For myotilin, it is therefore important to investigate potential roles of PIPs and known binding
441 partners like α-actinin-2. α-Actinin-2 recognises the 1-4-5-8 motif of the cognate α-actinin-2 "neck"
442 and/or titin Zr-7 by the pseudoligand mechanism regulated by PI(4,5)P_2. Our studies suggest that
443 myotilin binds to α-actinin-2 CAMD employing the same regulatory mechanism, setting the molecular
444 basis of interaction for the entire palladin family. In addition, our binding data suggest that titin can
445 displace myotilin from α-actinin-2, as titin Zr-7 interacts with α-actinin-2 with a stronger affinity (0.48
446 ± 0.13 μM) (7) than myotilin.

447 Furthermore, binding of PI(4,5)P_2 to α-actinin-2 downregulates its F-actin binding activity, resulting in
448 decreased F-actin cross-linking (52). In palladin PI(4,5)P_2 inhibits palladin-mediated F-actin
449 polymerization and cross-linking (48). By contrast, we showed that myotilin Ig1Ig2 does not bind
450 PI(4,5)P_2, however interactions with other parts cannot be completely excluded, suggesting that, as
451 opposed to α-actinin-2 and palladin, the myotilin:F-actin interaction is not regulated by PI(4,5)P_2. This
452 implies a possible mechanism for stabilization of α-actinin-2 on F-actin upon binding to myotilin:
453 PI(4,5)P_2 binding induces α-actinin-2 open conformation enabling it to interact with myotilin, while its
454 F-actin binding is simultaneously reduced due to PI(4,5)P_2. Concurrent binding of myotilin to α-actinin-
455 2 and F-actin can thus help to stabilize α-actinin-2 on F-actin and may compensate for the inhibitory
456 effect of PI(4,5)P_2.

457 Our SAXS data revealed full-length myotilin as a dynamic ensemble of multiple conformations with
458 local structurally compact clusters, as previously predicted based on sequence analysis (22). Further
459 local induction of structure might be promoted upon binding, in particular to α-actinin-2, similar to
460 titin and palladin where the interaction with CAMD of α-actinin-2 induces folding of the binding motif
461 into an α-helical structure (7,47,53).

462 Our studies of myotilin dimerization in solution revealed that the regions flanking Ig1Ig2 domains
463 enhance dimer stability. In comparison to the previous studies addressing myotilin dimerization
464 (9,10,17), we show that myotilin dimerizes in a concentration-dependent manner and that only
465 concentrations higher than 1.0 mM showed complete dimer population, implying a weak association.
466 This suggests mechanisms driving or stabilizing dimer formation *in vivo*: high local concentrations and
467 avidity effects mediated by concominat binding to interaction partners such as α-actinin, filamin C and
468 of course F-actin that teether myotilin to the Z-disc, and/or PTMs.

469 All known pathogenic myotilin variants result in a single residue substitution in the protein, and all,
470 except R405K, map to the N-terminus, within or close to the serine-rich region (SRR) and the
471 hydrophobic residues-rich region (HRR) representing its "mutational hotspot" (**Figure 1B**). These
472 mutations are predominantly substitutions from a polar/charged to a hydrophobic residue.

473 Consequently, in concert with the slower degradation and changed turnover as already indicated
474 previously (22,24), a newly exposed hydrophobic cluster could promote aggregation and play an
475 important role in pathological mechanisms. The R405K mutation in Ig2 was suggested to be
476 responsible for defective homo-dimerization of myotilin and decreased interaction with α-actinin-2
477 (27). However, our results revealed that R405K mutation does not impair myotilin homo-dimerization
478 *in vitro* (**Figure S1G**), nor does it affect the binding of myotilin to F-actin (**Figure 2A**), which was
479 expected since a positively charged residue is retained at this position. In addition, we predict this
480 mutation will not have an impact on binding of myotilin to α-actinin-2, since it does not reside in the
481 α-actinin-2 binding site or its proximity. Thus, further *in vitro* and *in vivo* experiments are needed to
482 understand the molecular mechanism underlying the pathophysiology caused by the R405K mutation.

483 An intriguing yet unresolved question is: how are the multitude of F-actin-binding proteins sorted
484 along thin myofilaments and Z-discs? Strikingly, tropomyosin is distributed all along thin filaments
485 except the Z-disc region (6). In non-muscle cells tropomyosin competes with α-actinin-1 and α-actinin-
486 4, for F-actin binding, resulting in mutually exclusive localizations along stress fibers (35,36). We reveal
487 that striated muscle-specific α-actinin-2 also competes with muscle type tropomyosin for binding to
488 F-actin, and thus extend the competition mechanism to all isoforms of α-actinin. Most importantly,
489 we found that myotilin also competes with tropomyosin for F-actin binding, and stabilizes F-actin
490 against depolymerization, suggesting it may be involved in excluding tropomyosin from the Z-disc.
491 Thus, binding of myotilin may create functionally distinct regions on actin filaments, thereby
492 modulating the interactions of other proteins with F-actin. However, myotilin alone does not explain
493 the absence of tropomyosin from the Z-disc. Instead, a concerted action of several Z-disc F-actin-
494 binding proteins (e.g. filamin C, α-actinin-2, ZASP, myotilin etc.) is required, which is supported by the
495 finding that the tropomyosin binding site on F-actin partly overlaps with the binding sites for filamin
496 C, α-actinin-2 and myotilin (**Figure S4C**). Sorting will be facilitated by local protein complex formation,
497 resulting in increased F-actin affinity, based on avidity effects. In this context it is noteworthy that
498 even a dramatic reduction of the binding strength of myotilin to F-actin, as shown by our FRAP
499 experiments, does not impair its Z-disc localization (**Figure 5**), supporting the view that the Z-disc is an
500 intricate network of interacting multidomain proteins, which may tolerate reduction or even loss of
501 individual interactions without attenuating the entire structure. This robustness rooted in redundancy
502 may also explain that the loss of a single protein by gene knockout may be compensated by other
503 proteins (54). Accordingly, the lack of a phenotype in myotilin knockout mice may be compensated by
504 myopalladin and/or palladin, which interact with EF34 hands of α-actinin-2 with similar affinity as
505 myotilin (47).

506 This raises the question of the role of myotilin in Z-disc biogenesis. According to current models, in
507 early myofibrillogenesis, premyofibrils are composed of minisarcomeres containing a subset of
508 sarcomeric proteins in α-actinin-2 enriched Z-bodies, whereas the attached thin filaments are
509 associated with tropomyosin and troponin (55). A recent study showed that tropomyosins are present
510 in sufficient levels in the cell to saturate all actin filaments (56). Therefore tropomyosin needs to be
511 actively inhibited from binding specific regions of the actin filaments to allow the formation of
512 tropomyosin-free actin filaments (56) necessary for the development of Z-discs. Myotilin is expressed
513 at relatively late stages of differentiation, when α-actinin-2, the Z-disc portion of titin,
514 myopodin/SYNPO2 and filamin C already co-localize at Z-bodies (10,57,58). Myotilin entry into this
515 still relatively loose protein assembly occurs at the time when mechanical strain increases due to
516 incipient contractile activity. Its simultaneous binding to F-actin and α-actinin, as well as the PIP_2-
517 dependent Zr7:α-actinin-2 interaction and the simultaneous displacement of tropomyosin make

518 myotilin an ideal co-organizer of Z-disc proteins (Figure 6). This timing seems essential since the longer
519 α-actinin molecules organize the more widely spaced F-actin networks required for myofibrils,
520 whereas myotilin alone would form too tightly packed filament bundles. Further studies are required
521 to determine the precise sequence of events regarding the assembly of components in maturing Z-
522 discs.

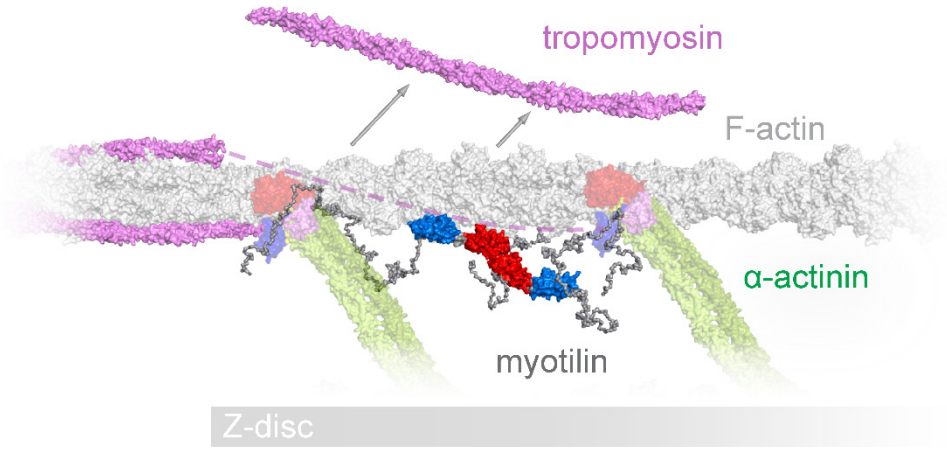

Figure 6. Model illustrating the role of myotilin in the organization of sarcomeric Z-disc assembly. Myotilin is recruited to the Z-disc by binding to F-actin, α-actinin-2 and/or other Z-disc components e.g. filamin C, ZASP, ect. As a part of the recruitment process, myotilin can further stabilise (in its proposed antiparallel dimeric form (10) two α-actinin-2 dimers on F-actin through interaction of its N-terminal region with CAMD of α-actinin-2. Consequently, together with α-actinin-2 and/or other Z-disc components, myotilin can help to displace tropomyosin from the Z-disc. For simplicity, only some of the Z-disc components are shown.

523

524 # Materials and methods

525 ## Plasmids and DNA constructs

526 Different DNA fragments, encoding human myotilin, or α-actinin-2 were sub-cloned into different
527 vectors as specified in Table S3. For preparation of myotilin mutants (Table S3), mutagenesis was
528 performed with the QuikChange II Site-Directed Mutagenesis Kit (Agilent). Trx-MYOT, $MYOT^{WT}$ and
529 $Ig1Ig2^{250-444}$ constructs were used as templates in the PCR reactions. Correct assembly of the prepared
530 constructs and mutagenesis efficiency was verified by DNA sequencing (GATC Biotech).

531

532 ## Protein expression and purification

533 All recombinant myotilin and α-actinin-2 constructs were expressed in *Escherichia coli* (see Table S3).
534 Full-length myotilin (Trx-MYOT) with N-terminal thioredoxin tag (Trx) and its mutant variant Trx-
535 MYOT-NEECK were expressed in B834 (DE3) grown at 37°C in LB media to an OD_{600} of approximately
536 1.0. Protein expression was induced by addition of IPTG to a final concentration of 0.5 mM and cells
537 were grown for additional 4-5 h at 37°C. Proteins were further purified by affinity chromatography
538 using HisTrap FF columns (Cytiva) followed by size exclusion chromatography (SEC) on a HiLoad 26/600

539 Superdex 200 column (Cytiva) equilibrated with 20 mM Tris, 400 mM NaCl, 250 mM arginine, 2 mM
540 β-mercaptoethanol, pH 7.5. Ig1Ig2$^{185-498}$ was expressed in C41 (DE3) strain following the protocol
541 described in (7) and purified by affinity chromatography using HisTrap FF columns. Subsequently, the
542 Trx-tag was cleaved overnight with HRV-3C protease added at a mass ratio protease:protein of 1:1000,
543 and the Ig1Ig2$^{185-498}$ was further purified by StrepTrap HP columns (Cytiva), followed by SEC on a
544 HiLoad 26/600 Superdex 75 column (Cytiva) equilibrated with 20 mM Tris, 150 mM NaCl, 5% glycerol,
545 pH 7.5.

546 During purification of Ig1Ig2$^{185-498}$*, the protein readily degrades from its C-terminus and forms
547 Ig1Ig2$^{185-454}$ as determined by intact protein mass spectrometry analysis of the final product. Thus to
548 prepare Ig1Ig2$^{185-454}$, Ig1Ig2$^{185-498}$* construct was expressed as described elsewhere (59). After
549 expression, cells were lysed by sonication and insoluble material removed by centrifugation. The
550 lysate was loaded onto a GSTrap FF column (Cytiva) equilibrated with 10 mM sodium phosphate, 140
551 mM NaCl, 2.7 mM KCl, pH 7.4 (PBS). After washing with the same buffer the bound proteins were
552 eluted by a linear gradient of 50 mM Tris, 10 mM reduced glutathione, pH 8.0. His$_6$-GST-tag was
553 removed by incubation with His$_6$-tagged TEV protease (added at a mass ratio protease:protein of
554 1:100) during overnight dialysis against the dialysis buffer (50 mM Tris, 150 mM NaCl, 1 mM DTT, pH
555 7.4) at 4°C. The His$_6$-GST-tag-free Ig1Ig2$^{185-454}$ was recovered as a flow-through after applying the
556 cleavage mixture onto Ni^{2+}-loaded HiTrap IMAC FF (Cytiva) and GSTrap FF columns to remove TEV
557 protease, uncleaved proteins, and the cleaved-off His$_6$-GST moiety. Final purification step was SEC on
558 a Superdex 75 10/300 column (Cytiva) equilibrated with 20 mM HEPES, 150 mM NaCl, 5% glycerol, 1
559 mM DTT, pH 7.4.

560 During expression, Ig1Ig2$^{250-498}$ degrades to Ig1Ig2$^{250-466}$ as verified by intact protein mass spectrometry
561 analysis. Thus, depending on the expression/purification strategy either Ig1Ig2$^{250-498}$ or Ig1Ig2$^{250-466}$ can
562 be prepared from cells expressing Ig1Ig2$^{250-498}$. To obtain Ig1Ig2$^{250-466}$ the expression and purification
563 procedure is basically the same as in (22) with the following differences: (1) for lysis buffer 20 mM
564 HEPES, pH 7.4, 150 mM NaCl, 5% glycerol, 10 mM imidazole was used, the lysate was applied to
565 HisTrap column and for elution the same buffer supplemented with 180 mM imidazole was used; (2)
566 cleavage with HRV-3C protease was done at protease:protein mass ratio 1:50 using 20 mM HEPES,
567 150 mM NaCl, 5% glycerol, pH 7.4; (3) the final SEC step was done using a HiLoad 16/600 Superdex 75
568 column (Cytiva) equilibrated with 20 mM HEPES, 150 mM NaCl, 5% glycerol, pH 7.2. This same
569 procedure is used to prepare Ig1Ig2$^{220-452}$, and Ig1Ig2$^{220-452\ R405K}$. To obtain Ig1Ig2$^{250-498}$, procedure was
570 the same as for Ig1Ig2$^{250-466}$, however protein expression was done in B834 (DE3) strain at 37°C for 3
571 h after induction with 0.5mM IPTG. In addition, before final SEC step, Ig1Ig2$^{250-498}$ was purified by
572 cation exchange chromatography using Resource S column (Cytiva) in 10 mM HEPES, 2 M urea, 5%
573 glycerol and gradient of 0-1 M NaCl, pH 7.0.

574 The Ig1Ig2$^{250-444}$ and all its mutant variants (see **Table S3**) were purified as described elsewhere (22).
575 The Ig1$^{250-344}$ and Ig2$^{349-459}$ constructs were purified as described in (59); the only modification was in
576 the final SEC step where the buffer was replaced by 20 mM HEPES, 150 mM, NaCl, 5% glycerol, 1 mM
577 DTT, pH 7.4.

578 Full-length α-actinin-2 constructs (ACTN2-WT and ACTN2-NEECK) were prepared as described
579 previously (7). ACTN2-EF14 was expressed as described in (7) and purified by affinity chromatography
580 using HisTrap FF columns. Subsequently, the His$_6$-tag was removed by incubation with HRV-3C
581 protease added at a mass ratio protease:protein of 1:50 during overnight dialysis against PBS, 5%

582 glycerol, 1 mM EDTA, 1 mM DTT at 4°C. The His_6-tag-free ACTN2-EF14 was recovered as a flow-through
583 after applying the cleavage mixture onto HisTrap FF column to remove HRV-3C protease, and
584 uncleaved proteins. Final purification step was SEC on a HiLoad 26/600 Superdex 75 column
585 equilibrated with PBS, 5% glycerol.

586 Palladin Ig3 was kindly provided by Moriah R. Beck (Wichita State University, Wichita, USA) and
587 prepared/purified as described in (48). Plasmid encoding constitutively monomeric mutant of actin
588 (DVD-actin) was kindly provided by Michael K. Rosen (University of Texas Southwestern Medical
589 Center, Dallas, USA) and protein was prepared as described in (31). Doc2b (49) and tropomyosin (34)
590 were kindly provided by Sascha Martens (Max Perutz Labs, University of Vienna, Vienna, Austria) and
591 Stefan Raunser (Max Planck Institute of Molecular Physiology, Dortmund, Germany), respectively.
592 Actin was prepared from rabbit skeletal muscle (60) and pyrene labeled following (61).

593

594 SAXS data collection and analysis

595 SEC-SAXS data collection of Trx-MYOT in 20 mM Tris, 400 mM NaCl, 250 mM arginine, 5% glycerol, pH
596 7.5 was conducted at the EMBL P12 beamline of the storage ring PETRA III (DESY, Hamburg, Germany)
597 (62) using an incident beam size of 200 × 110 μm^2 (FWHM) in a 1.7 mm quartz capillary held under
598 vacuum. For this, the set-up as described in (63) was employed. Here, an integrated micro splitter (P-
599 451, Upchurch Scientific) allows the eluent of a chromatography column (Superdex 200 increase
600 10/300 (Cytiva)) to flow equally through the SAXS capillary and a modular triple detector array (TDA,
601 Viscotek model TDA 305, Malvern Panalytical) that extracts MW estimates of SEC-separated
602 components by correlating refractive index (RI) and/or UV-vis concentrations with right angle laser
603 light data (RALLS) using the integrated Omnisec software (Malvern Panalytical). In parallel, 3000
604 individual SAXS frames were collected with 1 s exposure that were used for subsequent SAXS analysis.
605 The chromatography was conducted at 0.5 ml/min. SAXS data reduction to produce the final
606 scattering profile of monomeric Trx-MYOT was performed using standard methods. Briefly, 2D-to-1D
607 radial averaging was performed using the SASFLOW pipeline (64). Aided by the integrated prediction
608 algorithms in CHROMIXS, the optimal frames within the elution peak and the buffer regions were
609 selected (65). Subsequently, single buffer frames were subtracted from sample frames one by one,
610 scaled and averaged to produce the final subtracted curve which was further processed with various
611 programs from the ATSAS software package (64). Details on data collection are shown in **Table S1**.

612 SAXS data for purified myotilin constructs $Ig1Ig2^{250-444}$ and $Ig1Ig2^{250-498}$ was collected at ESRF beamline
613 BM29 BioSAXS (Grenoble, France) equipped with the Pilatus 1M detector. Samples were measured at
614 concentrations up to 14.12 ($Ig1Ig2^{250-444}$) or 42.8 mg/ml ($Ig1Ig2^{250-498}$) in 20 mM HEPES, 150 mM, NaCl,
615 5% glycerol, 1 mM DTT, pH 7.4, in two independent measurements. One SAXS dataset for the purified
616 myotilin construct $Ig1Ig2^{220-452}$ was collected at the EMBL X33 beamline of the storage ring Doris (DESY,
617 Hamburg, Germany) equipped with the Pilatus 1M-W detector at concentrations in the range from 1
618 to 52 mg/ml in 20 mM MES, 200 mM NaCl, 3 % glycerol, pH 6.0. The other SAXS dataset for the myotilin
619 construct $Ig1Ig2^{220-452}$ and the $Ig1Ig2^{220-452\ R405K}$ mutant was collected at EMBL P12 beamline of the
620 storage ring Petra III (DESY, Hamburg, Germany) equipped with the Pilatus 6M detector in the
621 concentration range 2.1-36.6 mg/ml ($Ig1Ig2^{220-452}$) and 2.3-45.5 mg/ml ($Ig1Ig2^{220-452\ R405K}$) in 20 mM
622 HEPES, 150 mM NaCl, 5 % glycerol, 1 mM DTT, pH 7.4. The momentum of transfer *s* is defined as
623 $s=4\pi\sin q/l$. Details on data collection are shown in **Table S1**. For all constructs background scattering
624 was subtracted, data reduced, normalised according to the measured concentration, and extrapolated

625 to infinite dilution using the two lowest measured concentrations using PRIMUS (66) module of the
626 ATSAS software package (64). Forward scattering (I_0) and radius of gyration (R_g) were obtained by
627 fitting the linear Guinier region of the data. Pair distribution function P(r) with the corresponding
628 maximum particle size parameter (D_{max}) was determined using GNOM program (67).

629 For reconstruction of a theoretical molecular envelope, *ab initio* modelling was performed 20 times
630 using the program DAMMIF (68), where scattering from the calculated envelopes was fitted against
631 the experimental scattering and evaluated by the chi values. The most typical envelope was selected
632 by comparing the normalised spatial discrepancy (NSD) values between pairs of envelopes and later
633 averaged by DAMAVER set of programs (69). In rigid body modelling, high resolution structures of
634 myotilin Ig1 (PDB: 2KDG) and Ig2 (PDB: 2KKQ) were used to fit SAXS scattering data using program
635 CORAL (70). Linker residues were designated as dummy atoms. *Ab initio* calculated envelope was
636 superposed to the rigid body model using SUPCOMB program (71).

637 Flexibility analysis for Trx-MYOT was performed using EOM 2.1 program (26) with enforced P1
638 symmetry while the linker between Ig domains was again designated as dummy atoms. To account
639 for the available information about the structure, the ensembles were generated as follows: during
640 the generation, the potentially flexible termini/domain were allowed to have randomized
641 conformations. Conformations consistent with scattering data were selected from the pool of 50 000
642 models using a genetic algorithm. The flexibility analysis was independently repeated three times; all
643 runs gave comparable results. One should, however, note that, for flexible macromolecules exploring
644 a range of conformations in solution, shape restoration returns average over the ensemble at a low
645 resolution of the model in **Figure 1D** of 56+/-4 Å. All structure figures were prepared using PyMOL
646 (The PyMOL Molecular Graphics System, version 2.3, Schrödinger, LLC). The SAXS data was deposited
647 at SASBDB, accession: SASDFZ7, SASDF28, SASDF38, SASDF48.

648

649 Cross-linking and mass spectrometry analyses

650 For cross-linking experiments with F-actin, actin was let to polymerize in PBS for 30 min at room
651 temperature before adding 4-(4,6-dimethoxy-1,3,5-triazin-2-yl)-4-methylmorpholiniumchloride
652 (DMTMM, MERCK) cross-linker. After incubation of F-actin with DMTMM for 5 min at room
653 temperature $Ig1Ig2^{250-444}$, or $Ig1Ig2^{185-454}$, or $Ig1Ig2^{185-498}$ in PBS was added at concentrations indicated
654 on the **Figure S3** and proteins were cross-linked for additional 40 min at room temperature. While for
655 cross-linking of $Ig1Ig2^{250-444}$, increasing concentrations of DMTMM were used (**Figure S3A**), fixed
656 concentration of DMTMM (2 mM) was used to cross-link $Ig1Ig2^{185-454}$ and $Ig1Ig2^{185-498}$ with F-actin
657 (**Figures S3B and S3C**). Following separation of cross-linking samples by SDS-PAGE and staining of
658 proteins with colloidal Coomassie Blue G-250, protein bands were excised, subjected to in-gel
659 digestion using trypsin and analyzed by HPLC–ESI–MS/MS using an UltiMate 3000 RSLCnano system
660 coupled to a Q Exactive Plus (both Thermo Fisher Scientific) mass spectrometer as described (72). For
661 identification of cross-linked peptides, the software pLink (73) was used, version 1.22 for $Ig1Ig2^{250-444}$
662 and $Ig1Ig2^{185-454}$, and version 2.0 for $Ig1Ig2^{185-498}$. For the former, MS raw data files were first converted
663 to the Mascot generic format (mgf) using msConvert from ProteoWizard, release 3.0.9740 (74).
664 Searches were performed against the forward and reversed amino acid sequences of the recombinant
665 proteins with parameters and filtering criteria as described previously (75). In brief, cross-linked
666 peptide matches were filtered at a false discovery rate (FDR) of 5%, and a minimum E-value of 5×10^{-2}
667 rejecting adjacent tryptic peptides of the same protein.

668

669 Actin co-sedimentation assays

670 Actin co-sedimentation assays were performed as was published in (76), with some modifications. As
671 various myotilin fragments displayed different solubility mostly depending on the pH of the buffer
672 used within the assay, co-sedimentation assays were performed at two different conditions, B1 and
673 B2. In the B1 conditions, rabbit skeletal muscle actin in G-buffer (2 mM HEPES, pH 8.0, 0.2 mM $CaCl_2$,
674 0.2 mM ATP, 2 mM β-mercaptoethanol) was polymerized with the addition of 1/10 volume of 10x F-
675 buffer (100 mM HEPES, pH 7.4, 500 mM KCl, 20 mM $MgCl_2$) and incubated for 30 min at room
676 temperature. Purified myotilin constructs $Ig1^{250-344}$, $Ig2^{349-459}$, $Ig1Ig2^{250-444}$ and its mutant variants were
677 dialyzed overnight against the dialysis buffer (20 mM HEPES, pH 7.4, 100 mM NaCl, 5% glycerol, 1 mM
678 DTT). For apparent dissociation constant determination, fixed concentration (16 µM) of myotilin
679 constructs in 20 µL of dialysis buffer was mixed with pre-polymerized F-actin (0-120 µM) in 20 µL of
680 1x F-buffer. For co-sedimentation with the increasing salt concentrations, pre-polymerized actin (6
681 µM) in 60 µL of 1x F-buffer was added to the myotilin construct in 60 µL of 1x F-buffer supplemented
682 with or without KCl to achieve a final concentration of 50, 100, 150, 250 and 300 mM. For
683 determination of binding of mutant myotilin variants to F-actin, pre-polymerized actin (8 µM) in 60 µL
684 of 1x F-buffer were added to the mutant myotilin variants (8 µM) in 60 µL of dialysis buffer. In the B2
685 conditions, the G-buffer was 2 mM PIPES, pH 6.8, 0.2 mM $CaCl_2$, 0.2 mM ATP, 5 mM β-
686 mercaptoethanol, 10x F-buffer consisted of 100 mM PIPES, 1 M NaCl, 10 mM $MgCl_2$, 10 mM EGTA, pH
687 6.8, and myotilin fragments Trx-MYOT, $Ig1Ig2^{250-444}$, $Ig1Ig2^{250-498}$, $Ig1Ig2^{185-454}$, and $Ig1Ig2^{185-498}$ were
688 dialyzed overnight against the 10 mM PIPES, 100 mM NaCl, 1 mM $MgCl_2$, 1 mM EGTA, 5% glycerol, pH
689 6.8. For determination of apparent dissociation constant(s) at B2 conditions, fixed concentration (6
690 µM) of myotilin fragment in 20 µL of dialysis buffer was mixed with pre-polymerized F-actin (0-60 µM)
691 in 20 µL of 1x F-buffer. Co-sedimentation assays with tropomyosin and Trx-MYOT or ACTN2-NEECK
692 mutant of α-actinin-2 were performed at B2 conditions as well. Here, Trx-MYOT (at final concentration
693 0-4.8 µM), or ACTN2-NEECK (0-6.0 µM) were mixed with pre-polymerized actin (6 µM) 30 min before
694 the addition of tropomyosin (2 µM), or tropomyosin (2 µM) was mixed with pre-polymerized actin (6
695 µM) 30 min before addition of Trx-MYOT (at final concentration 0-4.8 µM). Reaction mixtures in all
696 co-sedimentation assays were incubated at room temperature for 30 min prior to the
697 ultracentrifugation (125.000 x g, 30 min, 22°C). Pellets and supernatants were separated and equal
698 volumes analyzed by SDS-PAGE. Gels were scanned and quantified by densitometry with the
699 QuantiScan 1.5 software (Biosoft). For determination of dissociation constants, the amount of bound
700 myotilin constructs to F-actin in respect to free form was fitted with an equation for one site specific
701 binding using Prism 6 (GraphPad Software).

702

703 Preparation of liposomes and liposome co-sedimentation assay

704 Liposomes were prepared from chloroform stocks of 10 mg/ml of 1-palmitoyl-2-oleoyl-sn-glycero-3-
705 phosphocholine, POPC, 16:0-18:1 (Avanti Polar Lipids) and 1 mg/ml of porcine brain L-α-
706 phosphatidylinositol-4,5-bisphosphate, $PI(4,5)P_2$ (Avanti Polar Lipids). Lipid mixtures of 0-20% of
707 $PI(4,5)P_2$ and 80-100% of POPC were first dried under a stream of nitrogen, and then vacuum dried for
708 at least one hour. Dried lipid mixtures were hydrated in 20 mM Tris, 200 mM NaCl, 2% glycerol, 0.5
709 mM DTT, pH 8.5, incubated for 10 min at room temperature, gently mixed, further incubated for 20
710 min, and sonicated for 2 min at room temperature in a water bath, followed by 5 freezing-thawing

711 cycles. Using a mini-extruder (Avanti Polar Lipids), vesicles were then extruded through polycarbonate
712 filters with 0.4 µm and 0.1 µm pore sizes, respectively. In order to avoid the presence of potential
713 aggregates, the Ig3 domain of palladin, Ig1Ig2$^{250-444}$, and Doc2b, a positive control for PI(4,5)P_2 binding,
714 were first centrifuged in a TLA-55 rotor for 30 min at 100.000 x g, 4°C, using an optima MAX-XP
715 benchtop ultracentrifuge (Beckman Coulter Life Sciences). For the assay, proteins and liposomes were
716 mixed in polycarbonate tubes and incubated for 30 min at room temperature. Final concentrations of
717 liposomes and proteins were 0.5 mg/ml and 10 µM, respectively. Mixtures were ultracentrifuged in
718 TLA-100 rotor for 40 min at 100.000 x g, 20°C. Pellets and supernatants were separated and equal
719 volumes analyzed by SDS-PAGE. Gels were scanned and quantified by densitometry with the
720 QuantiScan 1.5 software (Biosoft).

721

722 NMR spectroscopy

723 For all NMR-based measurements uniformly ^{15}N-labelled constructs Ig1$^{250-344}$, Ig2$^{349-459}$ and Ig1Ig2^{250-}
724 ^{444} were expressed in *E. coli* BL21(DE3) using standard M9 minimal media. To generate protein
725 quantities amenable to ^{1}H-^{15}N HSQC based NMR studies, cell mass was generated in full media, before
726 switching to minimal media for induction (77). Protein purification was carried out as described above
727 (see Protein expression and purification). Assignments for the Ig1 and Ig2 domains of myotilin were
728 carried out previously and could be obtained from the Biological Magnetic Resonance Bank (Ig1, Entry
729 Number: 7113; Ig2, Entry Number: 16370).

730 Assignments were reviewed in the original measurement conditions and were then transferred to the
731 conditions used in this study by step gradients. For the construct Ig1Ig2$^{250-444}$ no assignments were
732 available and low expression yield was prohibitive to carrying out an assignment *de-novo*. Spectra of
733 all three forms were therefore simply overlaid, which enabled us to generate a partial assignment of
734 Ig1Ig2$^{250-444}$. This was possible as the two domains seem to fold independently of each other and also
735 do not show a dramatic change in shifts in the context of the full-length protein. A high affinity slowly
736 exchanging interaction of myotilin and F-actin would lead to a combined molecular mass well above
737 the NMR size limit. Weakly interacting species in fast exchange can, however, be measured on the
738 free form, which retains favourable tumbling times and still yields information on the bound form, as
739 the weighted average of the two species is detected. We thus used the shorter myotilin constructs
740 displaying the weakest affinity to F-actin, as well as single domains.

741 The interaction of Ig1$^{250-344}$, Ig2$^{349-459}$, Ig1Ig2$^{250-444}$ with F-actin was monitored using ^{1}H-^{15}N HSQC
742 measurements (78,79). Various concentrations were used in these experiments and are indicated in
743 the corresponding figure legends (**Figure S3D and S3E**). Both shift perturbations and changes in peak
744 intensity due to the addition of F-actin were followed. While intensity changes were monitored as a
745 simple ratio between the signal intensities (I_{bound}/I_{free}), shifts were tracked as a weighted average
746 between proton and nitrogen shift changes in peak centres. All figures show the root of the sum of
747 squared proton and nitrogen shifts in ppm values. While the proton shift is taken "as is", the nitrogen
748 shift is divided by a factor of five in order to reflect the fact that dispersion in the nitrogen dimension
749 is higher, while the achieved resolution is lower. Due to these circumstances, a diagonal shift has about
750 5 times higher changes in the nitrogen versus the proton dimension $shift = \sqrt{\Delta H^2 + (\frac{\Delta N}{5})^2}$. In
751 globular domains composed of β-sheets like Ig-domains of myotilin, chemical shift changes are
752 typically less localised and more dispersed on residues through the hydrogen-bonding network

753 stabilising adjacent β-strands in the β-sheet. We thus did not focus on individual residues, but rather
754 on segments of residues, which are part of the interaction interface. Shift averages showing shift-
755 patterns were therefore calculated by application of a rolling window average over 11 residues where
756 a minimum of 2 values were required to obtain a value for the average. The z-scores given express the
757 difference of the observed value (x) from the mean (μ) in terms of multiples of the standard deviation
758 (σ), i.e. $z = \frac{x-\mu}{\sigma}$. The average shift μ was calculated as a simple average $\frac{\sum_{i=1}^{n} x}{n}$. The standard deviation
759 σ was calculated as $\sigma = \sqrt{\frac{\sum_{i=1}^{n} (x-\mu)^2}{n-1}}$, n being the number of all observed values.

760

761 NMR measurements were carried out on Bruker Avance spectrometer at 800 MHz and 298 K. Samples
762 were prepared in 10 mM PIPES, 100 mM NaCl, 1 mM $MgCl_2$, 5% glycerol, pH 6.8 and D_2O was used at
763 a final concentration of 10% as the lock solvent. The only exception is the F-actin gradient with Ig1,
764 which was carried out in 10 mM imidazole, 50 mM KCl, 1 mM $MgCl_2$, 1 mM EGTA, pH 7.1.
765 Measurement at a single F-actin concentration at pH 6.8 confirms that the intensity changes and shifts
766 induced by F-actin are very similar in both conditions. Spectra were processed using NMRPipe (80). All
767 spectra recorded used Rance-Kay detected sensitivity enhanced Heteronuclear Single Quantum
768 Coherence sequences (HSQC) (78,79).

769

770 Macromolecular modeling

771 The $Ig1Ig2^{220-452}$ models displaying hypothetical dimer architectures were prepared by manually
772 moving two identical subunit copies where the Ig1 and Ig2 domains were in an extended relative
773 orientation. The two subunits were oriented in a way to mimic Ig-Ig interactions, which would support
774 dimer formation and to minimize steric clashes. These models were then used to calculate scattering
775 profile using Crysol (81), and *P(r)* using GNOM (67), both part the ATSAS software package (64).

776 For the model of myotilin:F-actin complex the model of tandem Ig1Ig2 domains in semi-extended
777 conformation based on SAXS data was used as a starting unbound structure (22). Linker residues
778 connecting myotilin Ig1 and Ig2 domains (residues 341-347), and N-terminal tail of actin (residues 3-
779 6) were designated as flexible. As a starting F-actin structure an actin dimer was used (PDB 3J8I). Initial
780 model was prepared by solvated docking implemented in Haddock 2.2 (32) using residues identified
781 by chemical cross-linking and co-sedimentation assays as restraints. The best model with regard to Z-
782 score was further refined using RosettaDock 2.3 (82) to yield the final myotilin:F-actin model.

783

784 Microscale thermophoresis

785 Microscale thermophoresis measurements were performed on the Monolith NT.115 (NanoTemper
786 Technologies) using fluorescently labelled DVD-actin. Purified DVD-actin was labelled using Monolith
787 NT protein labelling kit RED-NHS (Amine Reactive) dye (NanoTemper Technologies) according to the
788 manufacturer's instructions. The labelling reaction was performed in the supplied labelling buffer with
789 a concentration of 20 μM DVD-actin. The labelled DVD-actin was diluted to 80 nM with the reaction
790 buffer: 20 mM HEPES, 100 mM KCl, 0.1 mM $CaCl_2$, 0.2 mM ATP, 1 mM DTT, 5% glycerol, 0.2% Tween-
791 20, 0.5 mg/mL BSA, pH 8.0. Solutions of concentrated myotilin constructs were serially diluted in 2:1

792 ratio, with the same reaction buffer. 5 µL of labelled DVD-actin was added to the 15 µL of unlabelled
793 myotilin constructs. Reaction mixtures were incubated for 15 min at 25°C and approximately 5 µL of
794 solution was loaded into Monolith NT Standard Capillaries (NanoTemper Technologies).
795 Measurements were performed at 25°C using 20% LED and 20% IR-laser power with 5 s/30 s/5 s laser
796 off/on/off times. The myotilin dependent change in thermophoresis was described with a Hill function
797 to determine the apparent dissociation constant K_d of interaction from three independent
798 measurements.

799

800 F-actin depolymerization assays

801 Pyrene-labelled-F-actin filaments (30 µM, 25% pyrene labelled) were prepared by a 25 min incubation
802 at room temperature in buffer A (10 mM HEPES, 50 mM KCl, 2 mM $MgCl_2$, pH 8.0) in the presence or
803 absence of different concentrations of $Ig1Ig2^{250-444}$ (at molar ratios myotilin to actin as indicated on
804 **Figure 2E**). Depolymerization of actin filaments was induced by 100x dilution with buffer A to a final
805 concentration of 0.3 µM. Pre-cut pipet tips were used for all manipulations of actin filaments, and care
806 was taken to avoid filament shearing. Pyrene fluorescence was monitored at room temperature over
807 time at an excitation of 365 nm and emission of 388 nm in a Jasco FP-6300 fluorescence
808 spectrophotometer.

809

810 Transfection of myoblasts and fluorescence recovery after photobleaching

811 C2C12 cells were grown in proliferation medium [15% FCS, 100 U/ml penicillin, 100 µg/ml
812 streptomycin, 2 mM non-essential amino acids and 1 mM sodium pyruvate, in Dulbecco's modified
813 Eagle's medium (DMEM) with GlutaMAX]. Cells were trypsinized and transfected by nucleofection
814 according to the recommendations of the manufacturer (Lonza, Cologne, Germany) with N-terminal
815 EGFP-myotilin wild-type and mutants (K354A, K359A, K354/359A, K354/358/359A) (for details see
816 **Table S3**). After transfection, cells were seeded on glass coverslips (WPI, Berlin, Germany) in
817 proliferation medium. The medium was changed 24 h after transfection and cells were allowed to
818 differentiate at 90% confluence by changing the medium to differentiation medium (2% horse serum,
819 100 U/ml penicillin, 100 µg/ml streptomycin, 2 mM non-essential amino acids and 1 mM sodium
820 pyruvate, in DMEM with GlutaMAX). All media and supplements were from LifeTechnologies. Seven
821 days later FRAP experiments were performed using a Cell Observer Spinning Disk Confocal Microscope
822 (Carl Zeiss, Jena, Germany) equipped with an external 473 nm laser coupled via a scanner (UGA-40,
823 Rapp OptoElectronic, Hamburg, Germany). Cells were continuously kept at 37°C and 5% CO_2. Zen 2012
824 software was used for image processing. For FRAP analysis eight independent experiments were
825 performed. Regions of interest (ROI) were limited to a single Z-disc and for each cell 1-3 ROI were
826 chosen and bleached, for a pulse time of 1 ms with eight iterations, using the 473 nm laser (100 mW)
827 with 100% intensity. A series of three images was taken before bleaching. Immediately after
828 photobleaching, fluorescence recovery was monitored with an interval of 0.1 – 1 s until the signal was
829 fully recovered (300 s). The ImageJ package Fiji was used to determine the fluorescence intensity of
830 bleached and unbleached areas at each time point. Raw data were transformed into normalized FRAP
831 curves as previously described (83).

832

833 ## Isothermal titration calorimetry (ITC)

834 ITC experiments were performed at 25°C on a MicroCal PEAQ-ITC calorimeter (Malvern Panalytical).
835 Protein samples were dialyzed against 20 mM Hepes, 400 mM NaCl, 250 mM arginine, 5% glycerol,
836 pH 7.5. All solutions were degassed before the ITC experiments. Titrations consisted of sequential
837 injections, in which 400 µM of ACTN2-EF14 was added to a sample cell containing 20 µM of either Trx-
838 MYOT or Trx-MYOT-NEECK. The heats of dilution of ACTN2-EF14 into the buffer were determined
839 separately and subtracted from the titration prior to analysis. All data were analyzed using MicroCal
840 PEAQ-ITC analysis software (Malvern Panalytical).

841

842 ## Pull-down assay

843 Before each experiment, proteins were centrifuged at 100,000 × g for 30 min, 4°C. Trx-MYOT (5 µM)
844 was mixed with various α-actinin-2 constructs (2.5-7.5 µM, for details see **Figure 4F**) in 0.1 ml of buffer
845 P (20 mM Tris-HCl, 100 mM NaCl, 10 mM imidazole, 5% glycerol, pH 7.5) and incubated for 30 min at
846 room temperature. 25 µl of Co^{2+}-loaded Chelating Sepharose beads (Cytiva) were added to each
847 protein mixture, followed by incubation for 10 min at room temperature. After extensive washing with
848 buffer P, proteins bound to the beads were eluted with 50 mM Tris, 500 mM NaCl, 500 mM imidazole,
849 7 M urea, pH 8.0 and analysed by SDS-PAGE.

850

851 ## Differential scanning fluorimetry (DSF) assay

852 DSF was done following the protocol of (84) using a pH-screen described in (85). Briefly, a master mix
853 of protein/dye was prepared by mixing 420 µL of 0.5 mg/mL of Trx-MYOT with 2.1 µL 5000x SYPRO
854 Orange (Thermo Fisher Scientific) and filled up with 20 mM Tris, 400 mM NaCl, 250 mM arginine, 2
855 mM β-mercaptoethanol, pH 7.5 to 525 µL. 5 µL of the protein/dye master mix was added to each well
856 of 96-well PCR-plate containing 20 µL of the individual pH-screen solution (**Figure S2C**). The plate was
857 sealed, tapped to mix and centrifuged for 30 s at 1500 x g. For the stability screen, the temperature
858 was increased from 15°C to 95°C in 0.5°C (10 seconds hold time) increments. A fluorescence reading
859 was done every 0.5°C. Data analysis was performed using the CFX Manager software (Bio-Rad)
860 included with the RT-PCR machine.

861

862 # Data availability

863 The atomic coordinates have been deposited in the SASDB and are available with these links:

864 SASDFZ7

865 Full-length myotilin with N-terminally fused thioredoxin tag

866 https://www.sasbdb.org/data/SASDFZ7/4tm5723u5y/

867

868 SASDF28

Myotillin immuniglobulin domains Ig1Ig2 (220-452)

https://www.sasbdb.org/data/SASDF28/b0sfyy2m3k/

SASDF38

Myotillin immuniglobulin domains Ig1Ig2 (250-444)

https://www.sasbdb.org/data/SASDF38/knazhmxat5/

SASDF48

Myotillin immuniglobulin domains Ig1Ig2 (250-498)

https://www.sasbdb.org/data/SASDF48/w8mwgpml0d/

All other relevant data are described in SI Appendix or are available upon request. Full methods can be found in SI Appendix, Materials and Methods.

Author contributions

Conceptualization: KDC, JK, BL and DF; investigation: JK, MP, VP, TCS, FD, SM, MAG, CS, SS; writing (original draft): JK, MP, VP, TCS, FD, SM, MAG, SS, KDC; writing (review and editing): all authors.

Conflict of interests

The authors declare no conflict of interests.

Acknowledgements

We thank the staff of the SAXS beamline at ESRF in Grenoble and EMBL-Hamburg for their excellent support, especially Martin Schroer for his assistance with the SEC-SAXS/RALS set-up. This work was supported by the Slovenian Research Agency young researcher grant (No. 35337) and research program P1-0140. KDC research was supported by a Marie Curie Initial Training Network: MUZIC (N°238423), Austrian Science Fund (FWF) Projects I525, I1593, P22276, P19060 and W1221, Federal Ministry of Economy, Family and Youth through the initiative “Laura Bassi Centres of Expertise”, funding the Centre of Optimized Structural Studies, N°253275, by the Wellcome Trust Collaborative Award (201543/Z/16), COST action BM1405 - Non-globular proteins - from sequence to structure, function and application in molecular physiopathology (NGP-NET), WWTF (Vienna Science and Technology Fund) Chemical Biology project LS17-008, and by the University of Vienna.

This study was further supported by the Deutsche Forschungsgemeinschaft (DFG, German Research Foundation) FOR 1352 (projects P1, D.F.; and P4, B.W.) FOR 2743 (projects P6, D.F.; and P9, B.W.)

Project ID 403222702/SFB 1381 (project Z1, B.W.) and Germany's Excellence Strategy (CIBSS – EXC-2189 – Project ID 390939984, BW).

The FP7 WeNMR (project# 261572), H2020 West-Life (project# 675858) and the EOSC-hub (project #777536) European e-Infrastructure projects are acknowledged for the use of their web portals, which make use of the EGI infrastructure with the dedicated support of CESNET-MetaCloud, INFN-PADOVA, NCG-INGRID-PT, TW-NCHC, SURFsara and NIKHEF, and the additional support of the national GRID Initiatives of Belgium, France, Italy, Germany, the Netherlands, Poland, Portugal, Spain, UK, Taiwan and the US Open Science Grid.

S. Raunser (Max Planck Institute of Molecular Physiology, Dortmund, Germany), M. Beck (Wichita State University, USA), S. Martins (University of Vienna, AT) and M.K. Rosen (University of Texas Southwestern Medical Center, USA) are acknowledged for kindly providing clones and/or protein samples for human tropomyosin, Ig3 domain of human palladin, Doc2b and non-polymerizable *Drosophila melanogaster* DVD actin mutant, respectively. We thank Life Science Editors for editing assistance.

917 References

918 1. Janssen, I., Heymsfield, S. B., Wang, Z. M., and Ross, R. (2000) Skeletal muscle mass and
919 distribution in 468 men and women aged 18-88 yr. *J Appl Physiol (1985)* **89**, 81-88

920 2. Ulbricht, A., Eppler, F. J., Tapia, V. E., van der Ven, P. F., Hampe, N., Hersch, N., Vakeel, P.,
921 Stadel, D., Haas, A., Saftig, P., Behrends, C., Furst, D. O., Volkmer, R., Hoffmann, B., Kolanus,
922 W., and Hohfeld, J. (2013) Cellular mechanotransduction relies on tension-induced and
923 chaperone-assisted autophagy. *Current biology : CB* **23**, 430-435

924 3. Frank, D., and Frey, N. (2011) Cardiac Z-disc signaling network. *J Biol Chem* **286**, 9897-9904

925 4. Reimann, L., Wiese, H., Leber, Y., Schwable, A. N., Fricke, A. L., Rohland, A., Knapp, B., Peikert,
926 C. D., Drepper, F., van der Ven, P. F., Radziwill, G., Furst, D. O., and Warscheid, B. (2017)
927 Myofibrillar Z-discs Are a Protein Phosphorylation Hot Spot with Protein Kinase C (PKCalpha)
928 Modulating Protein Dynamics. *Mol Cell Proteomics* **16**, 346-367

929 5. Reimann, L., Schwable, A. N., Fricke, A. L., Muhlhauser, W. W. D., Leber, Y., Lohanadan, K.,
930 Puchinger, M. G., Schauble, S., Faessler, E., Wiese, H., Reichenbach, C., Knapp, B., Peikert, C.
931 D., Drepper, F., Hahn, U., Kreutz, C., van der Ven, P. F. M., Radziwill, G., Djinovic-Carugo, K.,
932 Furst, D. O., and Warscheid, B. (2020) Phosphoproteomics identifies dual-site phosphorylation
933 in an extended basophilic motif regulating FILIP1-mediated degradation of filamin-C. *Commun*
934 *Biol* **3**, 253

935 6. Luther, P. K. (2009) The vertebrate muscle Z-disc: sarcomere anchor for structure and
936 signalling. *J Muscle Res Cell Motil* **30**, 171-185

937 7. Ribeiro Ede, A., Jr., Pinotsis, N., Ghisleni, A., Salmazo, A., Konarev, P. V., Kostan, J., Sjoblom,
938 B., Schreiner, C., Polyansky, A. A., Gkougkoulia, E. A., Holt, M. R., Aachmann, F. L., Zagrovic, B.,
939 Bordignon, E., Pirker, K. F., Svergun, D. I., Gautel, M., and Djinovic-Carugo, K. (2014) The
940 structure and regulation of human muscle alpha-actinin. *Cell* **159**, 1447-1460

941 8. Young, P., and Gautel, M. (2000) The interaction of titin and alpha-actinin is controlled by a
942 phospholipid-regulated intramolecular pseudoligand mechanism. *EMBO J* **19**, 6331-6340

943 9. Salmikangas, P., Mykkanen, O. M., Gronholm, M., Heiska, L., Kere, J., and Carpen, O. (1999)
944 Myotilin, a novel sarcomeric protein with two Ig-like domains, is encoded by a candidate gene
945 for limb-girdle muscular dystrophy. *Hum Mol Genet* **8**, 1329-1336

946 10. Salmikangas, P., van der Ven, P. F., Lalowski, M., Taivainen, A., Zhao, F., Suila, H., Schroder, R.,
947 Lappalainen, P., Furst, D. O., and Carpen, O. (2003) Myotilin, the limb-girdle muscular
948 dystrophy 1A (LGMD1A) protein, cross-links actin filaments and controls sarcomere assembly.
949 *Hum Mol Genet* **12**, 189-203

950 11. Hauser, M. A., Horrigan, S. K., Salmikangas, P., Torian, U. M., Viles, K. D., Dancel, R., Tim, R.
951 W., Taivainen, A., Bartoloni, L., Gilchrist, J. M., Stajich, J. M., Gaskell, P. C., Gilbert, J. R., Vance,
952 J. M., Pericak-Vance, M. A., Carpen, O., Westbrook, C. A., and Speer, M. C. (2000) Myotilin is
953 mutated in limb girdle muscular dystrophy 1A. *Hum Mol Genet* **9**, 2141-2147

954 12. Gontier, Y., Taivainen, A., Fontao, L., Sonnenberg, A., van der Flier, A., Carpen, O., Faulkner,
955 G., and Borradori, L. (2005) The Z-disc proteins myotilin and FATZ-1 interact with each other
956 and are connected to the sarcolemma via muscle-specific filamins. *J Cell Sci* **118**, 3739-3749

957 13. von Nandelstadh, P., Ismail, M., Gardin, C., Suila, H., Zara, I., Belgrano, A., Valle, G., Carpen,
958 O., and Faulkner, G. (2009) A class III PDZ binding motif in the myotilin and FATZ families binds
959 enigma family proteins: a common link for Z-disc myopathies. *Mol Cell Biol* **29**, 822-834

960 14. Ruparelia, A., Vaz, R., and Bryson-Richardso, R. (2012) Myofibrillar Myopathies and the Z-Disk
961 Associated Proteins. in *Skeletal Muscle - From Myogenesis to Clinical Relations* (Cseri, J. ed.),
962 InTech, Croatia. pp 317-358

963 15. Selcen, D., and Engel, A. G. (2004) Mutations in myotilin cause myofibrillar myopathy.
964 *Neurology* **62**, 1363-1371

965 16. van der Ven, P. F., Wiesner, S., Salmikangas, P., Auerbach, D., Himmel, M., Kempa, S., Hayess,
966 K., Pacholsky, D., Taivainen, A., Schroder, R., Carpen, O., and Furst, D. O. (2000) Indications for
967 a novel muscular dystrophy pathway. gamma-filamin, the muscle-specific filamin isoform,
968 interacts with myotilin. *J Cell Biol* **151**, 235-248

969 17. von Nandelstadh, P., Gronholm, M., Moza, M., Lamberg, A., Savilahti, H., and Carpen, O.
970 (2005) Actin-organising properties of the muscular dystrophy protein myotilin. *Exp Cell Res*
971 **310**, 131-139

972 18. Dixon, R. D., Arneman, D. K., Rachlin, A. S., Sundaresan, N. R., Costello, M. J., Campbell, S. L.,
973 and Otey, C. A. (2008) Palladin is an actin cross-linking protein that uses immunoglobulin-like
974 domains to bind filamentous actin. *J Biol Chem* **283**, 6222-6231

975 19. Nakamura, F., Osborn, T. M., Hartemink, C. A., Hartwig, J. H., and Stossel, T. P. (2007)
976 Structural basis of filamin A functions. *The Journal of cell biology* **179**, 1011-1025

977 20. Otey, C. A., Dixon, R., Stack, C., and Goicoechea, S. M. (2009) Cytoplasmic Ig-domain proteins:
978 cytoskeletal regulators with a role in human disease. *Cell Motil Cytoskeleton* **66**, 618-634

979 21. Otey, C. A., Rachlin, A., Moza, M., Arneman, D., and Carpen, O. (2005) The
980 palladin/myotilin/myopalladin family of actin-associated scaffolds. *International review of*
981 *cytology* **246**, 31-58

982 22. Puz, V., Pavsic, M., Lenarcic, B., and Djinovic-Carugo, K. (2017) Conformational plasticity and
983 evolutionary analysis of the myotilin tandem Ig domains. *Sci Rep-Uk* **7**, 3993

984 23. Konrat, R. (2009) The protein meta-structure: a novel concept for chemical and molecular
985 biology. *Cell Mol Life Sci* **66**, 3625-3639

986 24. von Nandelstadh, P., Soliymani, R., Baumann, M., and Carpen, O. (2011) Analysis of myotilin
987 turnover provides mechanistic insight into the role of myotilinopathy-causing mutations.
988 *Biochem J* **436**, 113-121

989 25. Keduka, E., Hayashi, Y. K., Shalaby, S., Mitsuhashi, H., Noguchi, S., Nonaka, I., and Nishino, I.
990 (2012) In Vivo Characterization of Mutant Myotilins. *The American Journal of Pathology* **180**,
991 1570-1580

992 26. Tria, G., Mertens, H. D., Kachala, M., and Svergun, D. I. (2015) Advanced ensemble modelling
993 of flexible macromolecules using X-ray solution scattering. *IUCrJ* **2**, 207-217

994 27. Shalaby, S., Mitsuhashi, H., Matsuda, C., Minami, N., Noguchi, S., Nonaka, I., Nishino, I., and
995 Hayashi, Y. K. (2009) Defective myotilin homodimerization caused by a novel mutation in
996 MYOT exon 9 in the first Japanese limb girdle muscular dystrophy 1A patient. *J Neuropathol*
997 *Exp Neurol* **68**, 701-707

998 28. Beck, M. R., Dixon, R. D., Goicoechea, S. M., Murphy, G. S., Brungardt, J. G., Beam, M. T.,
999 Srinath, P., Patel, J., Mohiuddin, J., Otey, C. A., and Campbell, S. L. (2013) Structure and
1000 function of palladin's actin binding domain. *Journal of molecular biology* **425**, 3325-3337

1001 29. Jurrus, E., Engel, D., Star, K., Monson, K., Brandi, J., Felberg, L. E., Brookes, D. H., Wilson, L.,
1002 Chen, J., Liles, K., Chun, M., Li, P., Gohara, D. W., Dolinsky, T., Konecny, R., Koes, D. R., Nielsen,
1003 J. E., Head-Gordon, T., Geng, W., Krasny, R., Wei, G. W., Holst, M. J., McCammon, J. A., and

1004 Baker, N. A. (2018) Improvements to the APBS biomolecular solvation software suite. *Protein*
1005 *Sci* **27**, 112-128

1006 30. Marks, D. S., Hopf, T. A., and Sander, C. (2012) Protein structure prediction from sequence
1007 variation. *Nat Biotechnol* **30**, 1072-1080

1008 31. Zahm, J. A., Padrick, S. B., Chen, Z., Pak, C. W., Yunus, A. A., Henry, L., Tomchick, D. R., Chen,
1009 Z., and Rosen, M. K. (2013) The bacterial effector VopL organizes actin into filament-like
1010 structures. *Cell* **155**, 423-434

1011 32. van Zundert, G. C. P., Rodrigues, J., Trellet, M., Schmitz, C., Kastritis, P. L., Karaca, E.,
1012 Melquiond, A. S. J., van Dijk, M., de Vries, S. J., and Bonvin, A. (2016) The HADDOCK2.2 Web
1013 Server: User-Friendly Integrative Modeling of Biomolecular Complexes. *Journal of molecular*
1014 *biology* **428**, 720-725

1015 33. Heikkinen, O., Permi, P., Koskela, H., Carpen, O., Ylanne, J., and Kilpelainen, I. (2009) Solution
1016 structure of the first immunoglobulin domain of human myotilin. *J Biomol NMR* **44**, 107-112

1017 34. von der Ecken, J., Muller, M., Lehman, W., Manstein, D. J., Penczek, P. A., and Raunser, S.
1018 (2015) Structure of the F-actin-tropomyosin complex. *Nature* **519**, 114-117

1019 35. Gateva, G., Kremneva, E., Reindl, T., Kotila, T., Kogan, K., Gressin, L., Gunning, P. W., Manstein,
1020 D. J., Michelot, A., and Lappalainen, P. (2017) Tropomyosin Isoforms Specify Functionally
1021 Distinct Actin Filament Populations In Vitro. *Current biology : CB* **27**, 705-713

1022 36. Kemp, J. P., Jr., and Brieher, W. M. (2018) The actin filament bundling protein alpha-actinin-4
1023 actually suppresses actin stress fibers by permitting actin turnover. *J Biol Chem* **293**, 14520-
1024 14533

1025 37. Galkin, V. E., Orlova, A., Salmazo, A., Djinovic-Carugo, K., and Egelman, E. H. (2010) Opening
1026 of tandem calponin homology domains regulates their affinity for F-actin. *Nat Struct Mol Biol*
1027 **17**, 614-616

1028 38. Avery, A. W., Fealey, M. E., Wang, F., Orlova, A., Thompson, A. R., Thomas, D. D., Hays, T. S.,
1029 and Egelman, E. H. (2017) Structural basis for high-affinity actin binding revealed by a beta-III-
1030 spectrin SCA5 missense mutation. *Nat Commun* **8**, 1350

1031 39. Iwamoto, D. V., Huehn, A., Simon, B., Huet-Calderwood, C., Baldassarre, M., Sindelar, C. V.,
1032 and Calderwood, D. A. (2018) Structural basis of the filamin A actin-binding domain interaction
1033 with F-actin. *Nat Struct Mol Biol* **25**, 918-927

1034 40. Janco, M., Bonello, T. T., Byun, A., Coster, A. C., Lebhar, H., Dedova, I., Gunning, P. W., and
1035 Bocking, T. (2016) The impact of tropomyosins on actin filament assembly is isoform specific.
1036 *Bioarchitecture* **6**, 61-75

1037 41. Pollard, T. D. (2016) Actin and Actin-Binding Proteins. *Cold Spring Harb Perspect Biol* **8**

1038 42. Way, M., Pope, B., and Weeds, A. G. (1992) Evidence for functional homology in the F-actin
1039 binding domains of gelsolin and alpha-actinin: implications for the requirements of severing
1040 and capping. *J Cell Biol* **119**, 835-842

1041 43. Leinweber, B., Tang, J. X., Stafford, W. F., and Chalovich, J. M. (1999) Calponin interaction with
1042 alpha-actinin-actin: evidence for a structural role for calponin. *Biophys J* **77**, 3208-3217

1043 44. Risi, C., Eisner, J., Belknap, B., Heeley, D. H., White, H. D., Schroder, G. F., and Galkin, V. E.
1044 (2017) Ca(2+)-induced movement of tropomyosin on native cardiac thin filaments revealed by
1045 cryoelectron microscopy. *Proc Natl Acad Sci U S A* **114**, 6782-6787

1046 45. Atkinson, R. A., Joseph, C., Dal Piaz, F., Birolo, L., Stier, G., Pucci, P., and Pastore, A. (2000)
1047 Binding of alpha-actinin to titin: implications for Z-disk assembly. *Biochemistry* **39**, 5255-5264

1048 46. Ronty, M., Taivainen, A., Moza, M., Otey, C. A., and Carpen, O. (2004) Molecular analysis of
1049 the interaction between palladin and alpha-actinin. *FEBS letters* **566**, 30-34

1050 47. Beck, M. R., Otey, C. A., and Campbell, S. L. (2011) Structural characterization of the
1051 interactions between palladin and alpha-actinin. *Journal of molecular biology* **413**, 712-725

1052 48. Yadav, R., Vattepu, R., and Beck, M. R. (2016) Phosphoinositide Binding Inhibits Actin
1053 Crosslinking and Polymerization by Palladin. *Journal of molecular biology* **428**, 4031-4047

1054 49. Groffen, A. J., Martens, S., Diez Arazola, R., Cornelisse, L. N., Lozovaya, N., de Jong, A. P.,
1055 Goriounova, N. A., Habets, R. L., Takai, Y., Borst, J. G., Brose, N., McMahon, H. T., and Verhage,
1056 M. (2010) Doc2b is a high-affinity Ca2+ sensor for spontaneous neurotransmitter release.
1057 *Science* **327**, 1614-1618

1058 50. Wang, J., Dube, D. K., Mittal, B., Sanger, J. M., and Sanger, J. W. (2011) Myotilin dynamics in
1059 cardiac and skeletal muscle cells. *Cytoskeleton* **68**, 661-670

1060 51. Wang, J., Shaner, N., Mittal, B., Zhou, Q., Chen, J., Sanger, J. M., and Sanger, J. W. (2005)
1061 Dynamics of Z-band based proteins in developing skeletal muscle cells. *Cell Motil Cytoskeleton*
1062 **61**, 34-48

1063 52. Fraley, T. S., Tran, T. C., Corgan, A. M., Nash, C. A., Hao, J., Critchley, D. R., and Greenwood, J.
1064 A. (2003) Phosphoinositide binding inhibits alpha-actinin bundling activity. *J Biol Chem* **278**,
1065 24039-24045

1066 53. Atkinson, R. A., Joseph, C., Kelly, G., Muskett, F. W., Frenkiel, T. A., Nietlispach, D., and Pastore,
1067 A. (2001) Ca2+-independent binding of an EF-hand domain to a novel motif in the alpha-
1068 actinin-titin complex. *Nat Struct Biol* **8**, 853-857

1069 54. Moza, M., Mologni, L., Trokovic, R., Faulkner, G., Partanen, J., and Carpen, O. (2007) Targeted
1070 deletion of the muscular dystrophy gene myotilin does not perturb muscle structure or
1071 function in mice. *Mol Cell Biol* **27**, 244-252

1072 55. Sanger, J. W., Kang, S., Siebrands, C. C., Freeman, N., Du, A., Wang, J., Stout, A. L., and Sanger,
1073 J. M. (2005) How to build a myofibril. *J Muscle Res Cell Motil* **26**, 343-354

1074 56. Meiring, J. C. M., Bryce, N. S., Wang, Y., Taft, M. H., Manstein, D. J., Liu Lau, S., Stear, J.,
1075 Hardeman, E. C., and Gunning, P. W. (2018) Co-polymers of Actin and Tropomyosin Account
1076 for a Major Fraction of the Human Actin Cytoskeleton. *Current biology : CB* **28**, 2331-
1077 2337.e2335

1078 57. Linnemann, A., van der Ven, P. F., Vakeel, P., Albinus, B., Simonis, D., Bendas, G., Schenk, J. A.,
1079 Micheel, B., Kley, R. A., and Furst, D. O. (2010) The sarcomeric Z-disc component myopodin is
1080 a multiadapter protein that interacts with filamin and alpha-actinin. *European journal of cell*
1081 *biology* **89**, 681-692

1082 58. Mologni, L., Moza, M., Lalowski, M. M., and Carpen, O. (2005) Characterization of mouse
1083 myotilin and its promoter. *Biochem Biophys Res Commun* **329**, 1001-1009

1084 59. Drmota Prebil, S., Slapsak, U., Pavsic, M., Ilc, G., Puz, V., de Almeida Ribeiro, E., Anrather, D.,
1085 Hartl, M., Backman, L., Plavec, J., Lenarcic, B., and Djinovic-Carugo, K. (2016) Structure and
1086 calcium-binding studies of calmodulin-like domain of human non-muscle alpha-actinin-1. *Sci*
1087 *Rep-Uk* **6**, 27383

1088 60. Spudich, J. A., and Watt, S. (1971) The regulation of rabbit skeletal muscle contraction. I.
1089 Biochemical studies of the interaction of the tropomyosin-troponin complex with actin and
1090 the proteolytic fragments of myosin. *J Biol Chem* **246**, 4866-4871

1091 61. Kouyama, T., and Mihashi, K. (1981) Fluorimetry study of N-(1-pyrenyl)iodoacetamide-
1092 labelled F-actin. Local structural change of actin protomer both on polymerization and on
1093 binding of heavy meromyosin. *Eur J Biochem* **114**, 33-38

1094 62. Blanchet, C. E., Spilotros, A., Schwemmer, F., Graewert, M. A., Kikhney, A., Jeffries, C. M.,
1095 Franke, D., Mark, D., Zengerle, R., Cipriani, F., Fiedler, S., Roessle, M., and Svergun, D. I. (2015)
1096 Versatile sample environments and automation for biological solution X-ray scattering
1097 experiments at the P12 beamline (PETRA III, DESY). *J Appl Crystallogr* **48**, 431-443

1098 63. Graewert, M. A., Franke, D., Jeffries, C. M., Blanchet, C. E., Ruskule, D., Kuhle, K., Flieger, A.,
1099 Schafer, B., Tartsch, B., Meijers, R., and Svergun, D. I. (2015) Automated pipeline for
1100 purification, biophysical and x-ray analysis of biomacromolecular solutions. *Sci Rep-Uk* **5**,
1101 10734

1102 64. Franke, D., Petoukhov, M. V., Konarev, P. V., Panjkovich, A., Tuukkanen, A., Mertens, H. D. T.,
1103 Kikhney, A. G., Hajizadeh, N. R., Franklin, J. M., Jeffries, C. M., and Svergun, D. I. (2017) ATSAS
1104 2.8: a comprehensive data analysis suite for small-angle scattering from macromolecular
1105 solutions. *J Appl Crystallogr* **50**, 1212-1225

1106 65. Panjkovich, A., and Svergun, D. I. (2018) CHROMIXS: automatic and interactive analysis of
1107 chromatography-coupled small-angle X-ray scattering data. *Bioinformatics* **34**, 1944-1946

1108 66. Konarev, P. V., Volkov, V. V., Sokolova, A. V., Koch, M. H. J., and Svergun, D. I. (2003) PRIMUS:
1109 a Windows PC-based system for small-angle scattering data analysis. *Journal of Applied*
1110 *Crystallography* **36**, 1277-1282

1111 67. Svergun, D. I. (1992) Determination of the Regularization Parameter in Indirect-Transform
1112 Methods Using Perceptual Criteria. *Journal of Applied Crystallography* **25**, 495-503

1113 68. Franke, D., and Svergun, D. I. (2009) DAMMIF, a program for rapid ab-initio shape
1114 determination in small-angle scattering. *J Appl Crystallogr* **42**, 342-346

1115 69. Volkov, V. V., and Svergun, D. I. (2003) Uniqueness of ab initio shape determination in small-
1116 angle scattering. *Journal of Applied Crystallography* **36**, 860-864

1117 70. Petoukhov, M. V., Franke, D., Shkumatov, A. V., Tria, G., Kikhney, A. G., Gajda, M., Gorba, C.,
1118 Mertens, H. D. T., Konarev, P. V., and Svergun, D. I. (2012) New developments in the ATSAS
1119 program package for small-angle scattering data analysis. *Journal of Applied Crystallography*
1120 **45**, 342-350

1121 71. Kozin, M. B., and Svergun, D. I. (2001) Automated matching of high- and low-resolution
1122 structural models. *Journal of Applied Crystallography* **34**, 33-41

1123 72. Yilmaz, S., Drepper, F., Hulstaert, N., Cernic, M., Gevaert, K., Economou, A., Warscheid, B.,
1124 Martens, L., and Vandermarliere, E. (2016) Xilmass: A New Approach toward the Identification
1125 of Cross-Linked Peptides. *Anal Chem* **88**, 9949-9957

1126 73. Yang, B., Wu, Y. J., Zhu, M., Fan, S. B., Lin, J., Zhang, K., Li, S., Chi, H., Li, Y. X., Chen, H. F., Luo,
1127 S. K., Ding, Y. H., Wang, L. H., Hao, Z., Xiu, L. Y., Chen, S., Ye, K., He, S. M., and Dong, M. Q.
1128 (2012) Identification of cross-linked peptides from complex samples. *Nat Methods* **9**, 904-906

1129 74. Chambers, M. C., Maclean, B., Burke, R., Amodei, D., Ruderman, D. L., Neumann, S., Gatto, L.,
1130 Fischer, B., Pratt, B., Egertson, J., Hoff, K., Kessner, D., Tasman, N., Shulman, N., Frewen, B.,
1131 Baker, T. A., Brusniak, M. Y., Paulse, C., Creasy, D., Flashner, L., Kani, K., Moulding, C., Seymour,
1132 S. L., Nuwaysir, L. M., Lefebvre, B., Kuhlmann, F., Roark, J., Rainer, P., Detlev, S., Hemenway,
1133 T., Huhmer, A., Langridge, J., Connolly, B., Chadick, T., Holly, K., Eckels, J., Deutsch, E. W.,
1134 Moritz, R. L., Katz, J. E., Agus, D. B., MacCoss, M., Tabb, D. L., and Mallick, P. (2012) A cross-
1135 platform toolkit for mass spectrometry and proteomics. *Nat Biotechnol* **30**, 918-920

1136 75. Chan, A., Schummer, A., Fischer, S., Schroter, T., Cruz-Zaragoza, L. D., Bender, J., Drepper, F.,
1137 Oeljeklaus, S., Kunau, W. H., Girzalsky, W., Warscheid, B., and Erdmann, R. (2016) Pex17p-
1138 dependent assembly of Pex14p/Dyn2p-subcomplexes of the peroxisomal protein import
1139 machinery. *European journal of cell biology* **95**, 585-597

1140 76. Kostan, J., Salzer, U., Orlova, A., Toro, I., Hodnik, V., Senju, Y., Zou, J., Schreiner, C., Steiner, J.,
1141 Merilainen, J., Nikki, M., Virtanen, I., Carugo, O., Rappsilber, J., Lappalainen, P., Lehto, V. P.,
1142 Anderluh, G., Egelman, E. H., and Djinovic-Carugo, K. (2014) Direct interaction of actin
1143 filaments with F-BAR protein pacsin2. *EMBO Rep* **15**, 1154-1162

1144 77. Marley, J., Lu, M., and Bracken, C. (2001) A method for efficient isotopic labeling of
1145 recombinant proteins. *J Biomol NMR* **20**, 71-75

1146 78. Kay, L. E., Nicholson, L. K., Delaglio, F., Bax, A., and Torchia, D. A. (1992) Pulse Sequences for
1147 Removal of the Effects of Cross-Correlation between Dipolar and Chemical-Shift Anisotropy
1148 Relaxation Mechanism on the Measurement of Heteronuclear T1 and T2 Values in Proteins. *J*
1149 *Magn Reson* **97**, 359-375

1150 79. Palmer, A. G., Cavanagh, J., Wright, P. E., and Rance, M. (1991) Sensitivity Improvement in
1151 Proton-Detected 2-Dimensional Heteronuclear Correlation Nmr-Spectroscopy. *J Magn Reson*
1152 **93**, 151-170

1153 80. Delaglio, F., Grzesiek, S., Vuister, G. W., Zhu, G., Pfeifer, J., and Bax, A. (1995) NMRPipe: a
1154 multidimensional spectral processing system based on UNIX pipes. *J Biomol NMR* **6**, 277-293

1155 81. Svergun, D., Barberato, C., and Koch, M. H. J. (1995) CRYSOL– a Program to Evaluate X-ray
1156 Solution Scattering of Biological Macromolecules from Atomic Coordinates. *Journal of Applied*
1157 *Crystallography* **28**, 768-773

1158 82. Lyskov, S., and Gray, J. J. (2008) The RosettaDock server for local protein-protein docking.
1159 *Nucleic Acids Res* **36**, W233-238

1160 83. Leber, Y., Ruparelia, A. A., Kirfel, G., van der Ven, P. F., Hoffmann, B., Merkel, R., Bryson-
1161 Richardson, R. J., and Furst, D. O. (2016) Filamin C is a highly dynamic protein associated with
1162 fast repair of myofibrillar microdamage. *Hum Mol Genet* **25**, 2776-2788

1163 84. Mlynek, G., Lehner, A., Neuhold, J., Leeb, S., Kostan, J., Charnagalov, A., Stolt-Bergner, P.,
1164 Djinovic-Carugo, K., and Pinotsis, N. (2014) The Center for Optimized Structural Studies (COSS)
1165 platform for automation in cloning, expression, and purification of single proteins and protein-
1166 protein complexes. *Amino Acids* **46**, 1565-1582

1167 85. Mlynek, G., Kostan, J., Leeb, S., and Djinović-Carugo, K. (2019) Tailored Suits Fit Better:
1168 Customized Protein Crystallization Screens. *Crystal Growth & Design* **20**, 984-994

1169 86. Haywood, N. J., Wolny, M., Rogers, B., Trinh, C. H., Shuping, Y., Edwards, T. A., and Peckham,
1170 M. (2016) Hypertrophic cardiomyopathy mutations in the calponin-homology domain of
1171 ACTN2 affect actin binding and cardiomyocyte Z-disc incorporation. *Biochem J* **473**, 2485-2493

1172

1173

1174 # Supplementary Figures and Tables

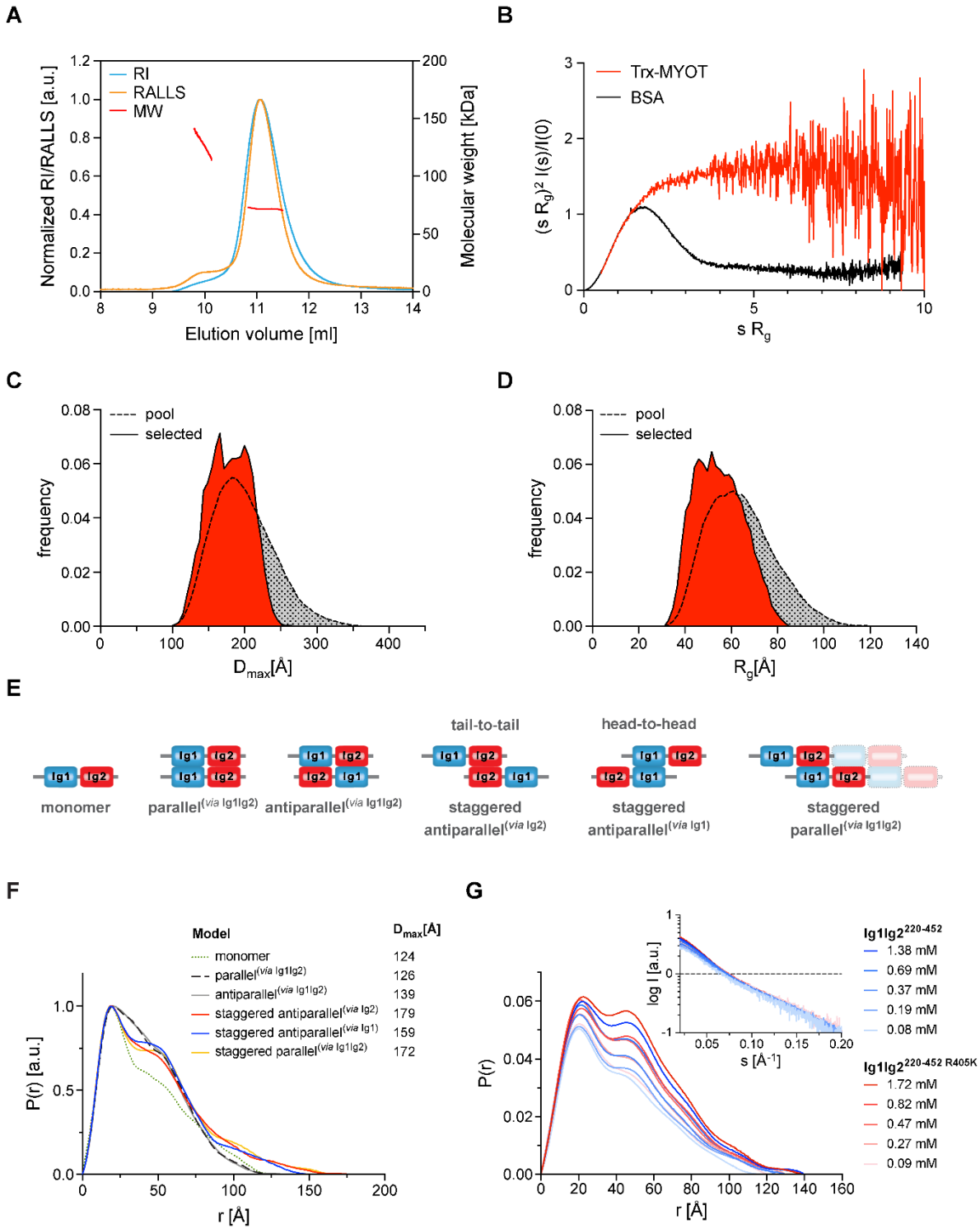

Figure S1. Related to Figure 1. Myotilin displays conformational ensemble in solution. (**A**) Determination of molecular weight (MW) across the RI/RALLS elution peak collected in parallel to SEC-SAXS mode. MW estimates are shown in red, right-angle laser light scattering (RALLS) trace in orange and refractive index (RI) trace in blue. The MW_{RALLS} (70 ± 7 kDa). MW estimates corresponding to elution time points prior to the main elution peak suggest a small presence of higher oligomeric species such as dimers. (**B**) Dimensionless Kratky plot indicates that while Trx-MYOT does contain ordered regions (corresponding to the Trx moiety and the Ig1 and Ig2 domains), most of the polypeptide chain is disordered and extended. In comparison, dimensionless Kratky plot of BSA, representing a typical folded protein, is shown. (**C, D**) D_{max} and R_g distributions from EOM analysis of Trx-MYOT. The parameters derived from the selected pool compared to the original pool suggest that Trx-MYOT is slightly restrictive in its flexibility and occupies a more compact conformation (EOM fit and models are shown in **Figures 1C and 1E**). (**E**) Schematic representation of $Ig1Ig2^{220-452}$ depicting potential modes of dimerization. (**F**) Theoretical *P(r) vs. r* plots calculated for potential $Ig1Ig2^{220-452}$ dimerization modes showed in (**E**). Of these, both parallel and antiparallel dimers using tandem Ig1Ig2 as dimerization interface (parallel$^{(via\ Ig1Ig2)}$, antiparallel$^{(via\ Ig1Ig2)}$) display marginal increase in the D_{max}. In the case of staggered parallel dimer (staggered parallel$^{(via\ Ig1Ig2)}$), dimerization could lead to formation of protein polymers, which were never observed within our experiments. Staggered antiparallel dimers (using either single Ig1 or Ig2 as dimerization interface) display notable increase in the D_{max} similar to experimentally observed (**Figure 1F and Table S1**), suggesting that staggered antiparallel dimerization mode of $Ig1Ig2^{220-452}$ is the most probable. In comparison to experimental data, where $Ig1Ig2^{220-452}$ adopts a conformational ensemble in solution (**Figure 1E**) (22), *P(r) vs. r* plots for different dimerization modes were calculated using one (static) conformation, consequently resulting in a longer D_{max} compared to experimentally derived. In order to compare various *P(r)* functions, *P(r)* was normalized to the peak height. (**G**) *P(r) vs. r* plot for the concentration series of $Ig1Ig2^{220-452}$ and $Ig1Ig2^{220-452\ R405K}$ measured at the same experimental conditions (for details see **Table S1**). Inset, respective concentration series with the corresponding SAXS profiles. Note, both $Ig1Ig2^{220-452}$ and $Ig1Ig2^{220-452\ R405K}$, showed comparable concentration dependent increase in D_{max} suggesting that *in vitro* R405K mutation does not impair myotilin homo-dimerization.

1175

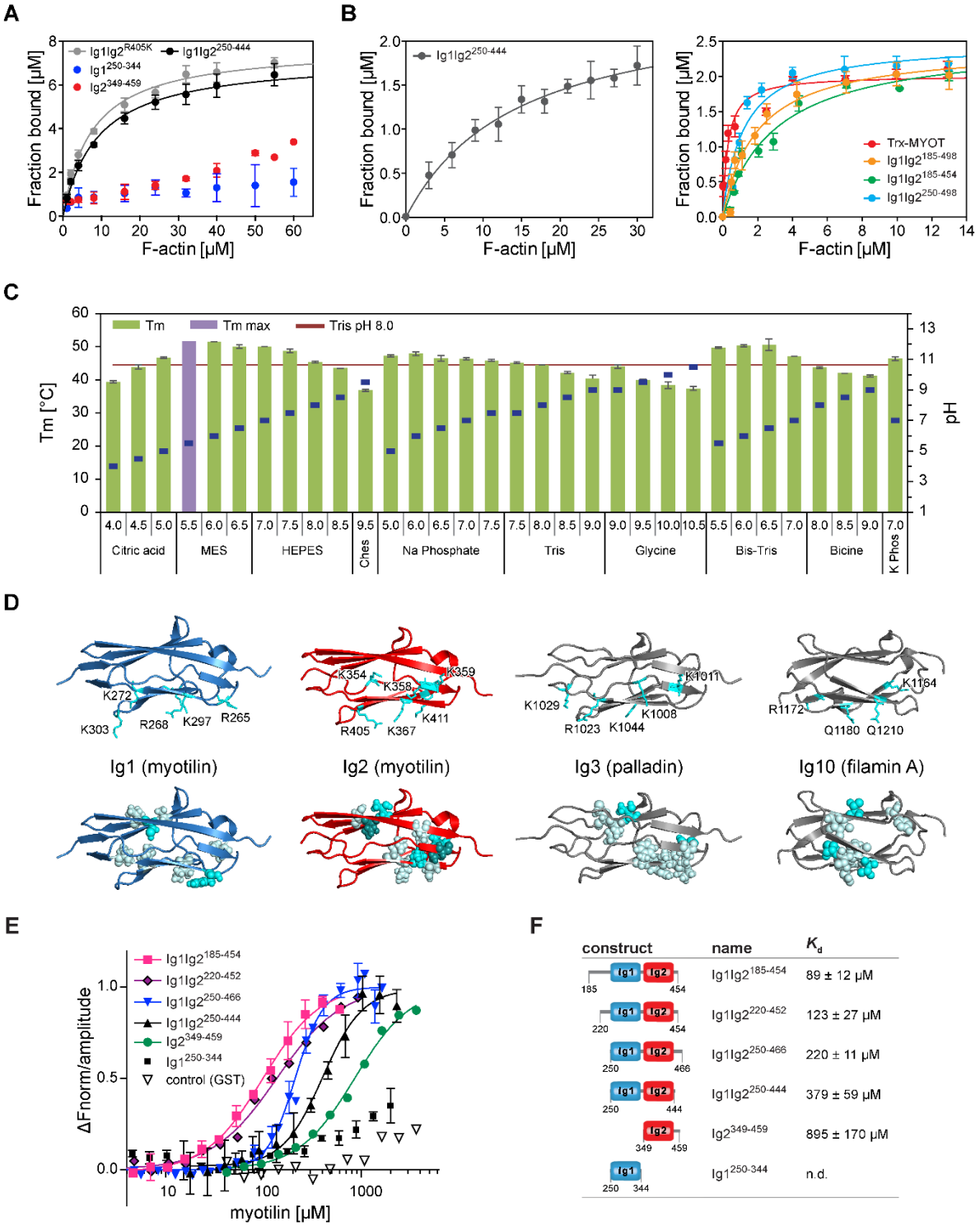
A
Fraction bound [µM]
F-actin [µM]
Ig1Ig2R405K
Ig1Ig2250-444
Ig1250-344
Ig2349-459
B
Ig1Ig2250-444
Trx-MYOT
Ig1Ig2185-498
Ig1Ig2185-454
Ig1Ig2250-498
C
Tm
Tm max
Tris pH 8.0
Tm [°C]
pH
Citric acid
MES
HEPES
Ches
Na Phosphate
Tris
Glycine
Bis-Tris
Bicine
K Phos
D
Ig1 (myotilin)
Ig2 (myotilin)
Ig3 (palladin)
Ig10 (filamin A)
E
ΔFnorm/amplitude
myotilin [µM]
Ig1Ig2185-454
Ig1Ig2220-452
Ig1Ig2250-466
Ig1Ig2250-444
Ig2349-459
Ig1250-344
control (GST)
F
construct
name
Kd
Ig1Ig2185-454 89 ± 12 µM
Ig1Ig2220-452 123 ± 27 µM
Ig1Ig2250-466 220 ± 11 µM
Ig1Ig2250-444 379 ± 59 µM
Ig2349-459 895 ± 170 µM
Ig1250-344 n.d.

Figure S2. Related to Figure 2. Myotilin binds to F-actin *via* Ig domains and disordered flanking regions and influences its dynamics. (**A, B**) Binding of various myotilin constructs to F-actin in conditions B1 (**A**) or conditions B2 (**B**). The exponential binding curves fitted for each set of data points were used to determine apparent binding affinities shown in **Figure 2A**. Plotted values represent the mean ± SEM from 3-5 independent experiments. (**C**) Melting temperature (T_m) of Trx-MYOT in various buffers as assessed by DSF assay (for details see Material and Methods). The pH of each buffer (blue rectangle) is indicated. T_m max (violet), denotes the buffer conditions in which T_m of Trx-MYOT was the highest (100 mM MES, pH 5.5). Brown line, indicates T_m in the standard buffer (100 mM Tris, pH 8.0). Note trend in increasing the stability of Trx-MYOT by lowering the pH. (**D**) Structural analysis of the functional (F-actin binding) sites on various Ig domains. Top panel: Basic amino acid residues with surface-exposed sidechains are shown as sticks (cyan). For palladin and filamin A this region corresponds to the F-actin binding region. Bottom panel: The functionally important residues as predicted by evolutionary coupling analysis and folding server EVfold (30) are shown as spheres, and coincide with the residues shown in the top panel on the lateral sides of the Ig domains. More intense (darker) color depicts a higher probability that the residue represents a functional site. (**E**) Binding of various myotilin constructs and control (GST) to fluorescently labelled monomeric DVD-actin measured by microscale thermophoresis (MST). (**F**) Table of the constructs and their affinity to DVD-actin obtained from the data shown in (**E**).

1176

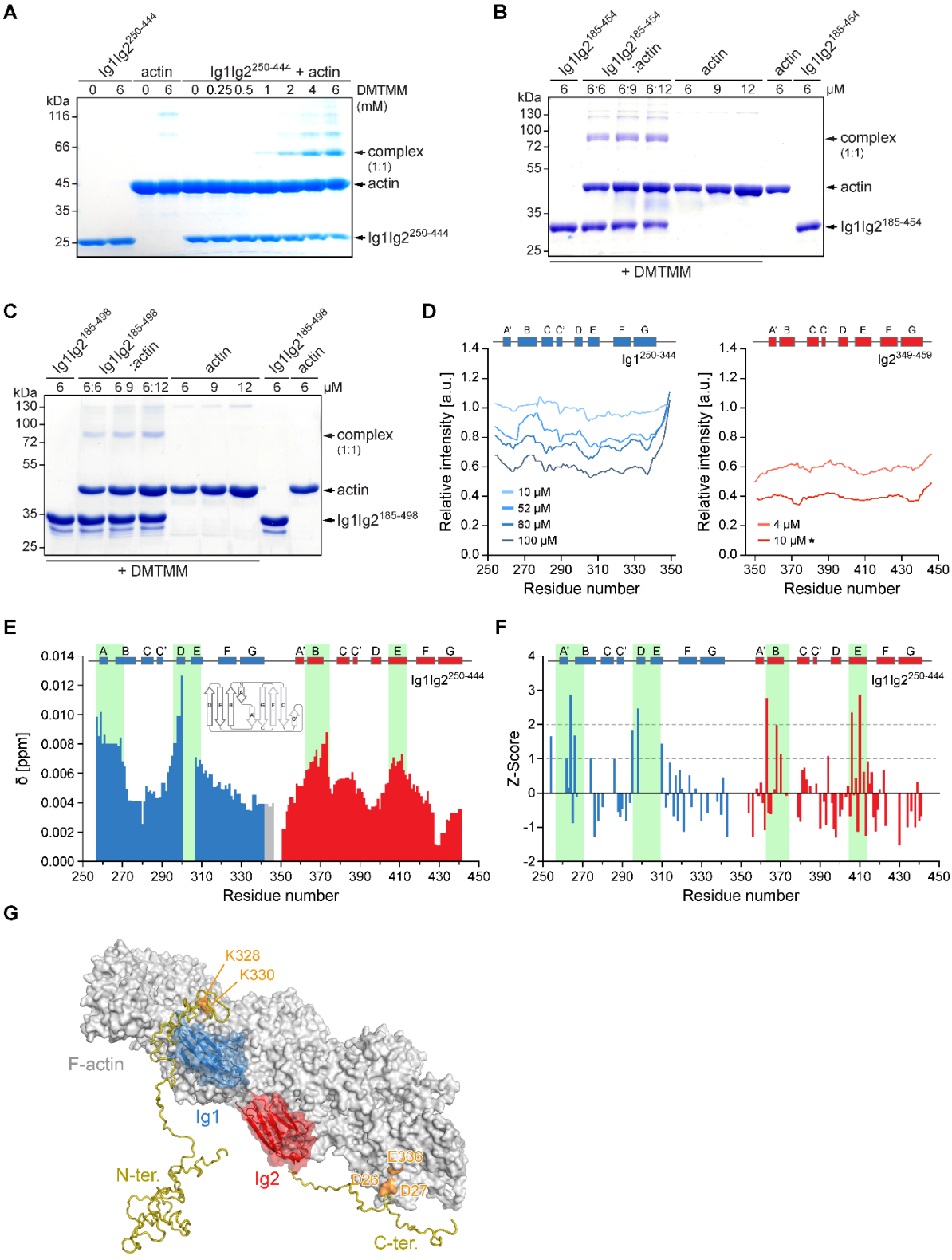
A
Ig1Ig2250-444
actin
Ig1Ig2250-444 + actin
0 6 0 6 0 0.25 0.5 1 2 4 6
DMTMM (mM)
kDa
116
66
45
35
25
complex (1:1)
actin
Ig1Ig2250-444
B
Ig1Ig2185-454
Ig1Ig2185-454 :actin
actin
actin
Ig1Ig2185-454
6 6:6 6:9 6:12 6 9 12 6 6
µM
kDa
130
100
72
55
35
25
complex (1:1)
actin
Ig1Ig2185-454
+ DMTMM
C
Ig1Ig2185-498
Ig1Ig2185-498 :actin
actin
Ig1Ig2185-498 actin
6 6:6 6:9 6:12 6 9 12 6 6
µM
kDa
130
100
72
55
35
25
complex (1:1)
actin
Ig1Ig2185-498
+ DMTMM
D
A' B C C' D E F G
Ig1250-344
Relative intensity [a.u.]
10 µM
52 µM
80 µM
100 µM
Residue number
Ig2349-459
4 µM
10 µM *
E
Ig1Ig2250-444
δ [ppm]
Residue number
F
Ig1Ig2250-444
Z-Score
Residue number
G
K328
K330
F-actin
Ig1
Ig2
N-ter.
E336
D26
D27
C-ter.

Figure S3. Related to Figure 3. Integrative model of myotilin:F-actin complex. (**A-C**) Cross-linking of myotilin $Ig1Ig2^{250-444}$ (**A**), $Ig1Ig2^{185-454}$ (**B**) and $Ig1Ig2^{185-498}$ (**C**) with F-actin. Myotilin-actin complexes were cross-linked with DMTMM, either at increasing concentrations of DMTMM and fixed amount of proteins ($Ig1Ig2^{250-444}$), or at its fixed concentration and varying amounts of proteins ($Ig1Ig2^{185-454}$ and $Ig1Ig2^{250-498}$). SDS-PAGEs of cross-linked samples stained with Coomassie Brilliant Blue are shown. Specific bands, corresponding to 1:1 complex were analyzed by MS and data obtained from it are summarized in **Table S2**. (**D**) Relative change of ^{1}H-^{15}N HSQC cross-peak intensities upon addition of F-actin to $Ig1^{250-344}$ (blue, left panel) or $Ig2^{349-459}$ (red, right panel). Values were averaged by a sliding window function over 11 amino acids. Stronger reduction in signal intensity of $Ig2^{349-459}$ as compared to $Ig1^{250-344}$ indicates that Ig2 binds more tightly to F-actin than Ig1. In all experiments, except for the one indicated by an asterisk (67 µM), a fixed concentration of myotilin was used (100 µM), while the concentration of F-actin was varied as indicated in the figure. (**E**) ^{1}H-^{15}N HSQC monitored shift changes in $Ig1Ig2^{250-444}$ (50 µM) upon addition of F-actin (4 µM). Shifts were averaged by a sliding window function over 11 amino acids. In $Ig1Ig2^{250-444}$ four main regions with the most pronounced effect upon addition of F-actin were identified (boxed green). Inset, topology diagram of I-type Ig domain. (**F**) Shifts used in (**E**) expressed using z-scores (see Materials and Methods for pertinent details on calculation of z-score). For all regions indicated in (**E**) we find more than one shift with a z-score above one and at least one higher than two.

1177

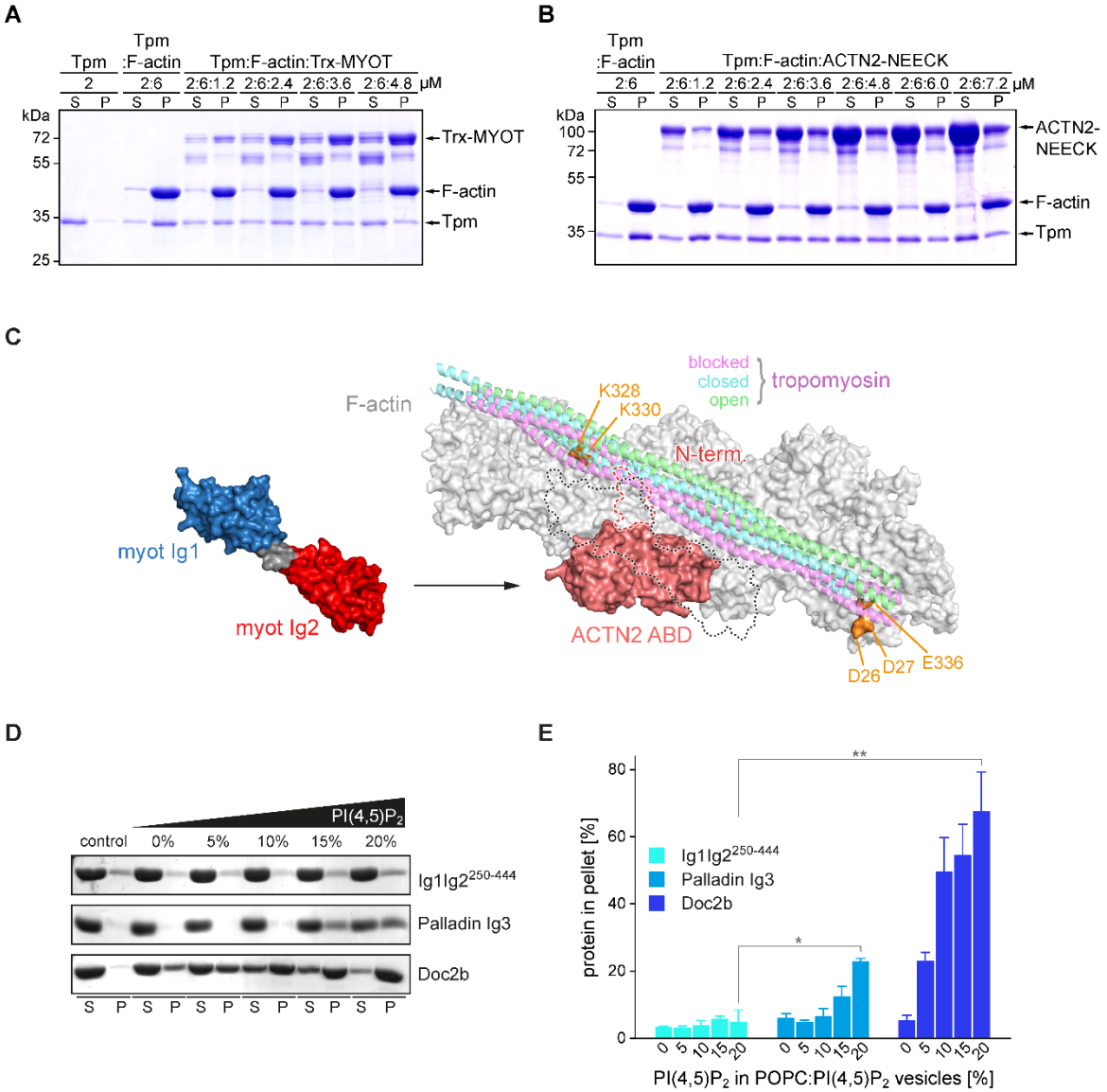
A
Tpm
Tpm
:F-actin
Tpm:F-actin:Trx-MYOT
2
2:6
2:6:1.2
2:6:2.4
2:6:3.6
2:6:4.8
μM
S P S P S P S P S P S P
kDa
72
55
35
25
Trx-MYOT
F-actin
Tpm
B
Tpm
:F-actin
Tpm:F-actin:ACTN2-NEECK
2:6
2:6:1.2
2:6:2.4
2:6:3.6
2:6:4.8
2:6:6.0
2:6:7.2
μM
S P S P S P S P S P S P S P
kDa
100
72
55
35
ACTN2-
NEECK
F-actin
Tpm
C
F-actin
blocked
closed
open
tropomyosin
K328
K330
N-term.
myot Ig1
myot Ig2
ACTN2 ABD
D26
D27
E336
D
PI(4,5)P2
control
0%
5%
10%
15%
20%
Ig1Ig2250-444
Palladin Ig3
Doc2b
S P S P S P S P S P S P
E
protein in pellet [%]
80
60
40
20
0
Ig1Ig2250-444
Palladin Ig3
Doc2b
**
*
0 5 10 15 20
0 5 10 15 20
0 5 10 15 20
PI(4,5)P2 in POPC:PI(4,5)P2 vesicles [%]
F
Myotilin Ig1 278APDVSWYLNGRTVQSD293
Myotilin Ig2 377PPKLFWKRNNEMVQFN390
Palladin Ig3 1029KPKIYWFKDGKQISPK1044

Figure S4. Related to Figure 4. Myotilin regulates binding of tropomyosin to F-actin and does not interact with PI(4,5)P_2. (**A**) Effects of myotilin on tropomyosin:F-actin interaction. Example of the SDS-PAGE used to generate **Figure 4B** is shown. Tropomyosin (Tpm) was incubated with F-actin before addition of Trx-MYOT at molar ratios indicated on the figure. F-actin and proteins bound were sedimented by centrifugation, and equal amounts of supernatant (S) and pellet (P) fractions were subjected to SDS-PAGE. (**B**) Effect of myotilin on α-actinin:F-actin interaction. Example of the SDS-PAGE used to generate **Figure 4D** is shown. α-Actinin-2 NEECK (ACTN2-NEECK) was incubated with F-actin before addition of tropomyosin (Tpm) at molar ratios indicated on the figure. F-actin and proteins bound were sedimented by centrifugation, and equal amounts of supernatant (S) and pellet (P) fractions were subjected to SDS-PAGE. (**C**) Model of tandem Ig domains of myotilin, actin binding domain of α-actinin-2 (ACTN2 ABD) and tropomyosin bound to F-actin was generated by superposition of our myotilin:tropomyosin:F-actin model shown on **Figure 4A** with the structures of F-actin bound to α-actinin-2, spectrin and filamin A, ABDs, at nominal resolutions of 16, 6.9 and 3.6 Å, respectively (37-39). In the next step, crystal structure of α-actinin-2 ABD (salmon color, PDB: 5A36) (86) was superimposed over ABD of filamin A (homologous to ABD of cardiac and skeletal muscles expressed isoform filamin C) to obtain the final model. Dotted line (black) indicates position of tandem Ig domains of myotilin (myot Ig1, myot Ig2) on F-actin as shown on **Figure 4A**. N-terminal regions preceding the ABDs increase affinity to F-actin and are isoform specific (38). The potential trace of the α-actinin-2 N-terminal extension (N-term.) on F-actin, as deduced from high resolution structures of F-actin decorated by filamin A and spectrin ABDs is shown with a dashed red line (39). In addition, actin-binding sites of α-actinin-2 and myotilin clearly overlap, explaining mutually exclusive binding of myotilin, α-actinin-2 and tropomyosin to F-actin. Residues of F-actin found in cross-links with N- and C-terminal regions flanking myotilin Ig domains are shown in orange (see **Figure 3A**). (**D** and **E**) Binding of myotilin to PI(4,5)P_2. Tandem of myotilin Ig domains (Ig1Ig2$^{250\text{-}444}$), Ig3 domain of palladin (Palladin Ig3) and double C2-like domain-containing protein beta (Doc2b) were incubated alone (control) or with different concentrations of PI(4,5)P_2 (0–20%) in POPC vesicles and centrifuged. Supernatant (S) and pellet (P) fractions obtained were separated on SDS-PAGE. (**D**) Representative gels from one of the three independent experiments are shown. (**E**) Quantitative representation of (**D**), where the amount of protein found in pellet (protein in pellet) is represented as the percentage of the total amount of the protein found in both supernatant and pellet fractions. Mean values (± SEM) of three independent experiments are shown. Significance was assessed using 2-tailed Student's *t*-test, *$p < 0.05$ and **$p < 0.01$. Note, myotilin does not bind to PI(4,5)P_2 containing vesicles. (**F**) Structural based sequence alignment of myotilin Ig1, myotilin Ig2 and palladin Ig3 domain. Residues that represent the putative PI(4,5)P_2 and Ins(1,4,5)P_3 binding sites on the Ig3 domain of palladin (48) are shown in green boxes. Conserved residues are shown in red. The numbers of the first and the last residue of the aligned sequences are given.

1178

Table S1: SAXS data collection, analysis and derived structural parameters

Construct	Ig1Ig2$^{250-444}$*	Ig1Ig2$^{250-498}$	Ig1Ig2$^{220-452}$	Trx-MYOT	Ig1Ig2$^{220-452}$†	Ig1Ig2$^{220-452\ R405K}$
Data collection parameters						
Radiation source	ESRF (Grenoble, France)		DESY (Hamburg, Germany)			
			Doris		Petra III	
Beamline	BM29 BioSAXS		EMBL X33	EMBL P12		
Detector	Pilatus 1M		Pilatus 1M-W	Pilatus 2M	Pilatus 6M	
Beam geometry [mm, FWHM]	0.10 × 0.20		n.d.	0.12 × 0.20	0.12 × 0.20	
Wavelength [nm]	0.099		0.126	0.124	0.124	
Sample–detector distance [m]	2.867		2.7	3.1	3.0	
Momentum of transfer *s* range [nm^{-1}]	0.04–4.0		0.1–6.0	0.08–3.5	0.15–7.3	
Exposure time [s]	15		15	1 (SEC-SAXS)	0.145	
Temperature [°C]	20		11	20	20	
Buffer	20 mM HEPES, 150 mM NaCl, 5% glycerol, 1 mM DTT, pH 7.4		20 mM MES, 200 mM NaCl, 3% glycerol, pH 6.0	20 mM Tris 400 mM NaCl, 250 mM arginine, 5% glycerol, pH 7.5	20 mM HEPES, 150 mM NaCl, 5% glycerol, 1 mM DTT, pH 7.4	
Overall parameters						
Conc. range measured$	1–14.12 mg/ml (0.05–0.64 mM)	1–42.8 mg/ml (0.04–1.53 mM)	1–52 mg/ml (0.04–1.96 mM)	n.a.	2.1–36.6 mg/ml (0.08–1.38 mM)	2.3–45.5 mg/ml (0.09–1.72 mM)
R_g (Guinier) [Å]	28 (0.64 mM)	32 (0.54 mM)	31 (0.04 mM)	51	30 (0.08 mM)	33 (0.09 mM)
		37 (1.53 mM)	37 (0.79 mM)		33 (0.19 mM)	34 (0.27 mM)
			39 (1.96 mM)		33 (0.37 mM)	34 (0.47 mM)
					34 (0.69 mM)	35 (0.82 mM)
					36 (1.38 mM)	36 (1.72 mM)
R_g from PDDF [Å]	29 (0.64 mM)	34 (0.54 mM)	32 (0.04 mM)	53	33 (0.08 mM)	34 (0.09 mM)
		38 (1.53 mM)	39 (0.79 mM)		34 (0.19 mM)	36 (0.27 mM)
			41 (1.96 mM)		35 (0.37 mM)	36 (0.47 mM)
					37 (0.69 mM)	37 (0.82 mM)
					37 (1.38 mM)	38 (1.72 mM)
D_{max} [Å]	101 (0.64 mM)	140 (0.54 mM)	107 (0.04 mM)	200	115 (0.08 mM)	120 (0.09 mM)
		152 (1.53 mM)	151 (0.79 mM)		125 (0.19 mM)	130 (0.27 mM)
			152 (1.96 mM)		130 (0.37 mM)	140 (0.47 mM)
					140 (0.69 mM)	140 (0.82 mM)
					140 (1.38 mM)	140 (1.72 mM)
M_w (RALLS) [kDa]	n.a.	n.a.	n.a.	70	n.a.	n.a.
M_w (DATMOV) [kDa]	24.3 (0.64 mM)	31.2 (0.54 mM)	27.3 (0.04 mM)	63.7	30.8 (0.08 mM)	29.1 (0.09 mM)
		44.7 (1.53 mM)	44.7 (0.79 mM)		30.7 (0.19 mM)	31.9 (0.27 mM)
			58.1 (1.96 mM)		33.7 (0.37 mM)	35.6 (0.47 mM)
					37.8 (0.69 mM)	40.6 (0.82 mM)
					43.2 (1.38 mM)	45.7 (1.72 mM)

(continued)

(continued)

Construct	**Ig1Ig2$^{250-444}$***	**Ig1Ig2$^{250-498}$**	**Ig1Ig2$^{220-452}$**	**Trx-MYOT**	**Ig1Ig2$^{220-452}$†**	**Ig1Ig2$^{220-452\ R405K}$**
M_w from Porod volume [kDa]	21.4 (0.64 mM)	26.4 (0.54 mM)	27.5 (0.04 mM)	77.3	26.9 (0.08 mM)	24.5 (0.09 mM)
		37.9 (1.53 mM)	36.7 (0.79 mM)		25.9 (0.19 mM)	26.3 (0.27 mM)
			48.2 (1.96 mM)		28.3 (0.37 mM)	29.6 (0.47 mM)
					30.9 (0.69 mM)	33.6 (0.82 mM)
					36.2 (1.38 mM)	38.2 (1.72 mM)
M_w (monomer sequence) [kDa]&	21.9	28.0	26.5	69.7	26.5	26.5
Software employed						
Primary data red.	SaxsAnalysis pipeline system			SASFLOW	SaxsAnalysis pipeline system	
Data processing	PRIMUS			PRIMUS / Cromixs	PRIMUS	
Calculation and comparison of scattering data	Crysol / Oligomer				n. a.	
Ab initio modelling	DAMMIF				n. a.	
Addition of missing residues	CORAL				n. a.	
Ensemble modelling	EOM				n. a.	
SASDB accession code	SASDF38	SASDF48	SASDF28	SASDFZ7		

*, the data for Ig1Ig2$^{250-444}$ were already measured and described previously (22)

$, for Ig1Ig2$^{250-498}$ and Ig1Ig2$^{220-452}$ structural parameters at various concentrations, relevant for the comparison, were calculated separately

&, M_w (monomer sequence) denotes molecular weight calculated from the amino acid sequence of the monomeric species

†, measured at the same experimental settings/conditions as Ig1Ig2$^{220-452\ R405K}$

1179
1180
1181

Table S2: List of major cross-links found between myotilin and F-actin (using DMTMM)

Myotilin constructs used	**(A)** Ig1 Ig2 250 444		**(B)** 185 Ig1 Ig2 454		**(C)** 185 Ig1 Ig2 498	
From Protein	**From Residue**	**To Protein**	**To Residue**	**Myotilin region**	**Myotilin fragment identified**	**Score**
myotilin	**K 474**	actin	**E 102**	C-ter.	C	212.6
myotilin	**K 462**	actin	**D 27**	C-ter.	C	199.5
myotilin	**K 411**	actin	**D 27***	Ig2	A, B	A) 157.5, B) 175.5
myotilin	**K 469**	actin	**E 102**	C-ter.	C	169.4
myotilin	**D 236**	actin	**K 330**	N-ter.	B, C	B) 138.4, C) 76.2
myotilin	**D 236**	actin	**K 328***	N-ter.	B	134.9
myotilin	**K 246**	actin	**E 336**	N-ter.	B, C	B) 105.9, C) 111.2
myotilin	**E 245**	actin	**K 330**	N-ter.	B	107.1
myotilin	**K 246**	actin	**D 26**	N-ter.	C	106.3
myotilin	**K 452**	actin	**D 27***	C-ter.	C	103.9
myotilin	**D 241**	actin	**K 330***	N-ter.	B	102.4
myotilin	**K 469**	actin	**D 26***	C-ter.	C	102.0
myotilin	**K 452**	actin	**D 26**	C-ter.	C	100.9
myotilin	**D 239**	actin	**K 330***	N-ter.	B	97.0
myotilin	**D 239**	actin	**K 328**	N-ter.	B	88.1
myotilin	**K 474**	actin	**D 27**	C-ter.	C	84.6
myotilin	**K 474**	actin	**E 336***	C-ter.	C	82.7
myotilin	**D 241**	actin	**K 328***	N-ter.	B	78.2
myotilin	**K 462**	actin	**D 26***	C-ter.	C	77.7
myotilin	**K 354**	actin	**D 27***	Ig2	C	76.7
myotilin	**K 246**	actin	**D 27***	N-ter.	B, C	B) 54.5, C) 73.9
myotilin	**K 415**	actin	**D 27**	Ig2	A, B	A) 66.1, B) 57.6
myotilin	**K 303**	actin	**D 27***	Ig1	A	65.9
myotilin	**K 367**	actin	**D 365**	Ig2	B	63.6
myotilin	**K 367**	actin	**E 366**	Ig2	B	60.2
myotilin	**K 452**	actin	**E 363**	C-ter.	C	48.2
myotilin	**K 411**	actin	**D 26**	Ig2	A	47.8
myotilin	**K 474**	actin	**D 26**	C-ter.	C	35.4

*, cross-links shown on Figure 3A; N-ter., region flanking Ig1Ig2 N-terminally; C-ter., region flanking Ig1Ig2 C-terminally; Score, computed as -10 log10 (E-value) representing best identification for a crosslink pair. The higher values of the score indicate more reliable identifications.

1182
1183
1184
1185

Table S3: List of constructs

Name	(1)Protein	Residues	Mutations	Vector	(2)Tag	Expression in	Origin
Trx-MYOT	myotilin	1-498	-	pETM-20	N-Trx-His_6-TEV	*E. coli*	this study
Trx-MYOT-NEECK	myotilin	1-498	F96E, L97E, L101E	pETM-20	N-Trx-His_6-TEV	*E. coli*	this study
Ig1Ig2$^{185-498}$	myotilin	185-498	-	pETM-20	N-Trx-His_6-3C C-Strep	*E. coli*	this study
(3)Ig1Ig2$^{185-498}$*	myotilin	185-498	-	pDB-HisGST	N-His_6-GST-TEV	*E. coli*	this study
Ig1Ig2$^{220-452}$	myotilin	220-452	-	pETM-14	N-His_6-3C	*E. coli*	this study
Ig1Ig2$^{220-452\ R405K}$	myotilin	220-452	R405K	pETM-14	N-His_6-3C	*E. coli*	this study
(4)Ig1Ig2$^{250-498}$	myotilin	250-498	-	pETM-14	N-His_6-3C	*E. coli*	this study
Ig1Ig2$^{250-444}$	myotilin	250-444	-	pETM-14	N-His_6-3C	*E. coli*	(22)
Ig1Ig2^{K354A}	myotilin	250-444	K354A	pETM-14	N-His_6-3C	*E. coli*	this study
Ig1Ig2^{Q356A}	myotilin	250-444	Q356A	pETM-14	N-His_6-3C	*E. coli*	this study
Ig1Ig2^{K358A}	myotilin	250-444	K358A	pETM-14	N-His_6-3C	*E. coli*	this study
Ig1Ig2^{K359A}	myotilin	250-444	K359A	pETM-14	N-His_6-3C	*E. coli*	this study
Ig1Ig2^{K367A}	myotilin	250-444	K367A	pETM-14	N-His_6-3C	*E. coli*	this study
Ig1Ig2^{R405K}	myotilin	250-444	R405K	pETM-14	N-His_6-3C	*E. coli*	this study
Ig1Ig2^{K411A}	myotilin	250-444	K411A	pETM-14	N-His_6-3C	*E. coli*	this study
Ig1Ig2$^{K354/359A}$	myotilin	250-444	K354A, K359A	pETM-14	N-His_6-3C	*E. coli*	this study
Ig1Ig2$^{K354/358/359A}$	myotilin	250-444	K354A, K358A, K359A	pETM-14	N-His_6-3C	*E. coli*	this study
Ig1$^{250-344}$	myotilin	250-344	-	pET-3d(+)	N-His_6-TEV	*E. coli*	this study
Ig2$^{349-459}$	myotilin	349-459	-	pET-3d(+)	N-His_6-TEV	*E. coli*	this study
MYOT^{WT}	myotilin	1-498	-	pEGFP-N1	N-EGFP	C2C12	this study
MYOT^{K354A}	myotilin	1-498	K354A	pEGFP-N1	N-EGFP	C2C12	this study
MYOT^{K359A}	myotilin	1-498	K359A	pEGFP-N1	N-EGFP	C2C12	this study
MYOT$^{K354/359A}$	myotilin	1-498	K354A, K359A	pEGFP-N1	N-EGFP	C2C12	this study
MYOT$^{K354/358/359A}$	myotilin	1-498	K354A, K358A, K359A	pEGFP-N1	N-EGFP	C2C12	this study
ACTN2-WT	α-actinin-2	1-894	-	pET-3d(+)	N-His_6-TEV	*E. coli*	(7)
ACTN2-NEECK	α-actinin-2	1-894	R268E, I269E, L273E	pET-3d(+)	N-His_6-TEV	*E. coli*	(7)
ACTN2-EF14	α-actinin-2	746-894	-	pETM-14	N-His_6-3C	*E. coli*	this study
palladin Ig3	palladin	1022-1126	-	pTBSG	N-His_6-TEV	*E. coli*	(48)
Doc2b	Doc2b	125-412	-	pGEX4T1	N-GST-Thr	*E. coli*	(49)
DVD-actin	actin-5C	1-376	D287A, V288A, D289A	pFastBacHT	N-His_6	*Sf9*	(31)
tropomyosin	tropomyosin					*E. coli*	(34)

(1), myotilin (human, Uniprot-ID Q9UBF9); α-actinin-2 (human, P35609), palladin (Mus musculus, Q9ET54), Doc2b (Rattus norvegicus, P70610), actin-5C (Drosophila melanogaster, P10987), tropomyosin (Tpm1.1st, Homo sapiens, NP_001018005.1)
(2), in many cases removed during purification; N, N-terminal fusion; Trx, Thioredoxin-tag; His_6, 6xHis-tag, TEV; TEV protease cleavage site; 3C, HRV-3C protease cleavage site; C, C-terminal fusion; Strep, Strep-tag II; Thr, thrombin cleavage site, GST, Glutathione s-transferase-tag; EGFP, Enhanced green fluorescent protein-tag
(3), Ig1Ig2$^{185-498}$* was used to produce Ig1Ig2$^{185-454}$, and GST
(4), Ig1Ig2$^{250-498}$ was used to produce Ig1Ig2$^{250-466}$

1186